LITHOS 406–407 (2021) 106541

Contents lists available at ScienceDirect

LITHOS

journal homepage: www.elsevier.com/locate/lithos

The role of mantle and crust in the generation of calc-alkaline Variscan magmatism and its tectonic setting in the Eastern Pyrenees

M. Liesa [a,*], C. Aguilar [a,b], A. Castro [c], G. Gisbert [d], J. Reche [e], J.A. Muñoz [f], M. Vilà [g]

[a] Departament de Mineralogia, Petrologia i Geologia Aplicada, Universitat de Barcelona, Zona Universitària de Pedralbes, 08028 Barcelona, Spain
[b] Centre for Lithospheric Research, Czech Geological Survey, 11821 Praha 1, Czech Republic
[c] Instituto Andaluz de Ciencias de la Tierra (IACT), Consejo Superior de Investigaciones Científicas–Universidad de Granada (CSIC-UGR), Avenida de las Palmeras, 4, 18100 Armilla, Granada, Spain
[d] Instituto de Geociencias (IGEO), Consejo Superior de Investigaciones Científicas-Universidad Complutense de Madrid (CSIC-UCM), Ciudad Universitaria, 28040 Madrid, Spain
[e] Departament de Geologia, Universitat Autònoma de Barcelona, 08193 Bellaterra (Cerdanyola del Vallès), Barcelona, Spain
[f] Institut de Recerca Geomodels, Departament de Dinàmica de la Terra i de l'Oceà, Universitat de Barcelona, Zona Universitària de Pedralbes, 08028 Barcelona, Spain
[g] Institut Cartogràfic i Geològic de Catalunya, Barcelona, Spain

ARTICLE INFO

Keywords:
Mafic–mantle origin rocks
Granite petrogenesis
P–T conditions
Granite emplacement mechanisms
Pyrenees
Variscan orogen

ABSTRACT

The lower structural levels of the Variscan orogen exposed in the Eastern Pyrenees reveal three genetically associated magmatic suites: (i) a batholitic sized calc-alkaline granitoid (Sant Llorenç – La Jonquera, SL–LJ); (ii) minor mafic intrusions with local ultramafic cumulates (Ceret and Mas Claret mafic complexes); and (iii) peraluminous leucogranite bodies. These suites were emplaced in a *syn*- to post-collisional setting during the Late Carboniferous – Early Permian (ca. 315–290 Ma) in an Upper Proterozoic-Upper Ordovician metasedimentary sequence. We carried out field and petrographic work and whole-rock geochemistry (including Sr—Nd radiogenic isotopes) in order to constrain the petrogenetic relationships between them and to determine the interplay of the igneous suites with the country rock. We compare geochemical data to those from the neighbouring massifs of the Pyrenees and Catalan Coastal Ranges. The granitoids and the mafic complexes underwent variable degrees of lower crustal assimilation as demonstrated by the Sr and Nd isotopic ratios of SL–LJ granitoids and mafic rocks. Contaminated gabbro-diorites are high in Fe and Zr and contain magmatic garnet in equilibrium with an Fe—Mg amphibole. A supra-subduction metasomatized mantle source for the mafic complexes is inferred. The magma that formed the SL–LJ granitoids was of intermediate composition and may have formed by differentiation of of magmas derived from partial melting of a subduction-metasomatized mantle caused by active subduction or mantle delamination or by partial melting of the lower crust triggered by underplating of mantle-derived mafic magmas. Leucogranite magmas formed later by partial melting of crustal rocks with compositions similar to the outcropping metapelites and orthogneisses. We deduce a retrograde cooling decompression path from 0.75 GPa down to 0.55 GPa from phase equilibria for a garnet-bearing diorite. This path is compatible with a local extensional context linked to a regional dextral strike-slip regime that provided space for the ascent and emplacement of the pluton. This strike-slip system is consistent with late-Variscan shear zones displacing Gondwana to the west with respect to Laurasia during the orogenic collapse.

1. Introduction

Large I-type granitic (sensu lato) plutons are typical constituents of the cores of active continental margins and collisional orogens. They are composed of a suite of tonalite, granodiorite, and subordinate granite (Castro, 2020), and are commonly associated with smaller intrusions of basic and intermediate rocks, as well as leucogranites. There is still debate on the origin of I-type granites, but two main generation mechanisms are considered (see Castro, 2020 and references therein): 1) differentiation of subduction-related mantle-derived basaltic to

Abbreviations: SL, Sant Llorenç; LJ, La Jonquera.

* Corresponding author.
E-mail addresses: mliesa@ub.edu (M. Liesa), carmenmaguilar@ub.edu (C. Aguilar), antonio.castro@csic.es (A. Castro), joan.reche@uab.cat (J. Reche), jamunoz@ub.edu (J.A. Muñoz), miquel.vila@icgc.cat (M. Vilà).

https://doi.org/10.1016/j.lithos.2021.106541
Received 19 February 2021; Received in revised form 11 November 2021; Accepted 11 November 2021
Available online 16 November 2021

andesitic magmas (Cordilleran-type magmas, typical of active continental margins) and 2) partial melting of lower crust triggered by underplating of mantle-derived mafic magmas (Caledonian-type magmas, typical of the late stages of collisional orogens). Lower crustal granulites were suggested to constitute the refractory residue of Caledonian-type water-undersaturated melts (Roberts et al., 2000). Conversely, granulites may represent cumulates produced during differentiation of Cordilleran-type magmas that will become the subsequent source of Caledonian-type melts (Castro, 2013; Castro, 2020). Leucogranites constitute anatectic melts of middle to upper crustal origin or extremely fractionated melts from the dominant magma and may form during different stages of the orogeny.

Both Cordilleran- to Caledonian-type granitic rocks as well as associated basic and intermediate intrusions have calc-alkaline major and trace element arc-related compositions. Suites of multiple intrusions with a wide rock spectrum offer us clues for understanding the processes taking place in the mantle and at the base of the crust, such as the degree of partial melting in the source area (Hall, 1966), the amount of water the magmas contained, the modification of the composition of the magma by differentiation (Brophy, 1991), or the variable interaction with the hosting continental crust, mainly through assimilation. The presence of recycled crustal components may be recorded in the mineralogy and the geochemistry of the igneous rocks (Hamilton and Myers, 1967). For instance, garnet is a common accessory phase in peraluminous magmas, but it is an unusual phase in metaluminous intermediate-basic rocks (Narduzzi et al., 2017 and references therein). It is generally related to magma contamination although its origin in igneous rocks may vary. Its stability mostly depends on *P*, *T*, and composition (Clarke, 1981), thus it gives valuable information on formation conditions of igneous rocks.

Three distinct magmatic suites are characteristic of late Variscan magmatism throughout the Iberian massif, the Pyrenees and the Catalan Coastal Chains (e.g., Castro, 2020; Vilà et al., 2005): (i) calc-alkaline granitoids forming up to several hundred km^2 plutons; (ii) mafic complexes occurring as small intrusions (from decametric bodies up to stocks of tens of km^2); and (iii) anatectic S-type granites and migmatites. Mafic complexes include high Mg—K rocks and high Fe rocks. High Mg—K rocks are generally associated with post-collisional granitic rocks (Couzinié et al., 2014; Janoušek et al., 1997; Scarrow et al., 2009) and are considered markers of the end of the orogeny. This rock association forms the appinitic series and may be used to gain insight into the role of the mantle transferring either mass or heat to the crust (Couzinié et al., 2014; Galán et al., 2017; Janoušek et al., 1997). The high Fe rocks are generally related to crustal contamination by mantle derived magmas.

In the Pyrenees (Fig. 1a), a wide crustal section of the Variscan orogen is preserved in the inner domains of the Pyrenean Alpine belt (Muñoz, 1992). Magmatic rocks were emplaced in a *syn*- to post-collisional setting during the Late Carboniferous – Early Permian (ca. 315 to 290 Ma; e.g., Cocherie, 1984; Roberts et al., 2000; Maurel, 2003; Aguilar et al., 2014; Druguet et al., 2014) in metasedimentary country rocks which range in age from the Upper Proterozoic in the Eastern Pyrenees to Carboniferous in the West (Fig. 1a). Granitoids intruded at upper crustal levels whereas mafic rocks were emplaced either in the upper crust or in the middle crust (e.g., Aguilar et al., 2015; Debon et al., 1995; Liesa and Carreras, 1989; Olivier et al., 2016; Vilà et al., 2005). The biggest intrusions (e.g., Maladeta, Andorra-Mont-Lluís, Querigut-Millars, Sant Llorenç – La Jonquera among others; Fig. 1a) consist of calc-alkaline plutons of tonalite, granodiorite, quartz-monzodiorite and monzogranite compositions. Mafic complexes are generally composed of gabbro, diorite and tonalite, and minor ultramafic rocks. All rock types are amphibole-bearing and in ultramafic rocks amphibole oikocrysts include olivine. They may be related to mantle-derived hydrated magmas and may be involved in the formation of the granitoids as suggested in the Iberian massif (Galán et al., 2017). Mafic rocks are either located inside the granitoids or near the outer contacts (such as the Boí gabbro, in La Maladeta pluton or the Mas Claret mafic complex in the Sant Llorenç – La Jonquera pluton; Fig. 1b) or crop out as isolated bodies in contact with metasedimentary rocks (such as the Farallons quartz diorite in the Cap de Creus massif or the Ceret mafic complex in Sant Llorenç – La Jonquera pluton; Fig. 1b). Leucogranites are usually found as dykes or small plutons which crosscut granitic plutons, the mafic complexes, and the metasedimentary country rocks.

The present work is focused on the calc-alkaline Sant Llorenç – La Jonquera pluton (SL–LJ), the Ceret and Mas Claret mafic complexes, and a swarm of leucogranites, located in the easternmost Pyrenees (Fig. 1a). No comprehensive studies of the pluton had been undertaken prior to this study, although studies on different aspects were carried out in previous works (Aguilar et al., 2014, 2015, 2016; Cocherie, 1984; Estévez, 1973; Liesa, 1994; Liesa and Carreras, 1989; Maurel, 2003; Olivier et al., 2016; Vilà et al., 2005, 2007). In this study, we acquired new field and petrographic data and performed whole rock major and trace element analysis, radiogenic isotope geochemistry and mineral chemistry, together with phase equilibria modeling, in order to constrain the petrogenetic relationships between the three igneous suites and to determine their origin. Understanding the ultimate causes of mafic magmatism in the region will shed light on the origin of belt-scale processes during and after the Variscan orogeny. The field relationships and the geometry of the SL–LJ pluton, as well as the associated mafic complexes, complement the geochemical study to help interpret the emplacement mechanism and the prevailing tectonic regime during the late stages of the Variscan orogeny in the Eastern Pyrenees. There is no any other metamorphic and gneissic dome in the Pyrenean Axial Zone where the geometric relationships between granitoids and the different structural levels of the Variscan crust (Fig. 1) are so clearly depicted. Moreover, the antiform geometry permits the observation of the Alpine imprint.

2. Geological setting

The Sant Llorenç – La Jonquera pluton (SL–LJ) and the Ceret and Mas Claret mafic complexes were emplaced in a mainly metasedimentary sequence from the Roc de Frausa and L'Albera massifs (Fig. 1b). This sequence is dominated by Upper Proterozoic to Upper Ordovician – Silurian metapelitic and metagreywackic rocks interbedded with several orthogneiss sheets (Aguilar et al., 2015; Baudin et al., 2009; Liesa and Carreras, 1989; Vilà et al., 2005, 2007). The gneiss sheets are located near the base of the Upper Proterozoic – Mid Ordovician sequence and represent pre-Variscan granites intruded at 560 ± 7 Ma (Mas Blanc orthogneiss; Castiñeiras et al., 2008), 476 ± 5 Ma (Roc de Frausa orthogneiss; Castiñeiras et al., 2008) and 470 ± 3 Ma (L'Albera orthogneiss; Liesa et al., 2011). They are all crosscut by a wealth of younger leucogranite dykes or small plutons (e.g., El Castellar pluton) (Liesa and Carreras, 1989; Vilà et al., 2005).

The pre-Variscan rocks were affected by two main Variscan deformation events (D1 and D2, described in detail in Liesa and Carreras, 1989; Vilà et al., 2007 and Aguilar et al., 2015) associated with regional metamorphism. D1 is responsible for a pervasive foliation (S1) which is axial plane of folds affecting the bedding. S1 is the dominant structure shown by the metamorphic rocks throughout the area. D2 deformation phase is related to NE-SW folds of D1 and a local foliation (S2) was generated in the deeper crustal levels (Fig. 1c). Contact metamorphism occurred around Variscan magmatic intrusions (Aguilar et al., 2015, 2016). The metasedimentary units preserve a continuous L*P*–H*T* metamorphic sequence which locally reached anatexis. Migmatites were formed both in the lowermost outcropping crustal levels associated with regional metamorphism as well as surrounding mafic intrusions (contact migmatites) at mid crustal levels (Aguilar et al., 2015, 2016). Metamorphic *P*–*T* conditions for the metapelitic units were constrained in the L'Albera Massif at 0.25 GPa and 400 °C for the biotite zone, 0.28 GPa and 535 °C for the andalusite-cordierite zone and 0.33 GPa and 625 °C for the sillimanite zone (Vilà et al., 2007). In the Roc de Frausa Massif, Aguilar et al. (2015) calculated ~0.45–0.26 GPa and 580–640 °C for the

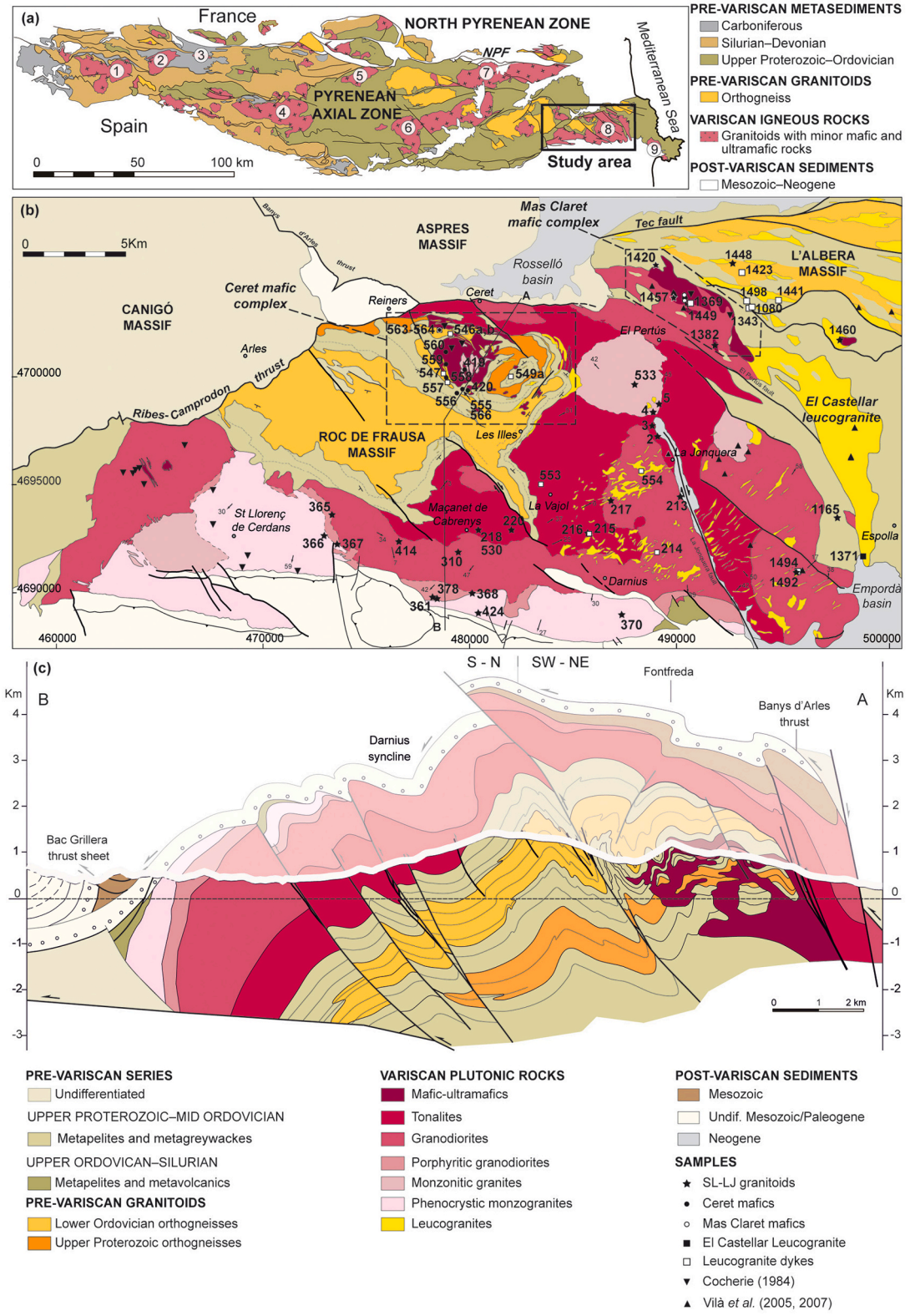

Fig. 1. (a) Geological sketch map of the Variscan segment of the Central and Eastern Pyrenees (the study area is outlined). The main Carboniferous plutons of the Pyrenees are: (1) Cauterets, (2) Neouvielle, (3) Bordères-Louron, (4) Maladeta, (5) Bassiès, (6) Andorra – Mont-Lluís, (7) Querigut – Millars, (8) Sant Llorenç – La Jonquera and (9) Roses – Rodes. (b) Geological map of the Sant Llorenç – La Jonquera (SL–LJ) pluton, associated mafic complexes, and leucogranites. Modified from Liesa and Carreras (1989), Vilà et al. (2005) and Baudin et al. (2009). S1 foliation dip data as well as representative foliation traces have been sketched in the Roc de Frausa metasediments and gneisses. Mineral lineations of the magmatic fabric from Olivier et al. (2016) are represented in SL–LJ pluton. Locations of samples collected for this study and samples from Vilà et al. (2005, 2007) and Cocherie (1984) are indicated. (c) N-S cross-section accross the SL–LJ pluton and the Roc de Frausa massif. It has been constructed by down-plunge projection taking as a reference the folds and bedding attitudes of the Paleocene sediments unconformably overlying the Variscan rocks. At the southern boundary of SL–LJ pluton, a non-outcropping fault has been interpreted as an extensional early Permian fault as suggested by the upper Paleozoic rocks in the hangingwall and the volcanic rocks interpreted as Permian in age by Baudin et al. (2009).

sillimanite zone and ~ 0.5–0.3 GPa and ~ 730 °C for the migmatites of the deeper levels affected by regional metamorphism. The age of Variscan regional metamorphism was estimated to be 320 ± 13 Ma and 315 ± 4 Ma (conventional U—Pb zircon ages by SHRIMP-RG; Aguilar et al., 2014) for a regional migmatite of the lower crustal level.

A subsequent deformation event (D3) affected all pre-Variscan and Variscan rocks of the area. The geometry of the main cartographic patterns, as well as the present antiformal geometry, results from a fold interference pattern produced by D2 and D3 folding phases (Fig. 1c). The antiformal geometry is shown by the whole Roc de Frausa massif, the SL-LJ granitoid and the post-Variscan rocks (Triasic and Paleocene) unconformably overlying the granitoid to the north, east, and south of the massif. To the North, the lower Triassic sandstones unconformably overly the high-grade metamorphic rocks of the Upper-Proterozoic-Lower Cambrian succession, whereas, to the South, the low metamorphic grade Upper Paleozoic rocks constitute the southern contact of

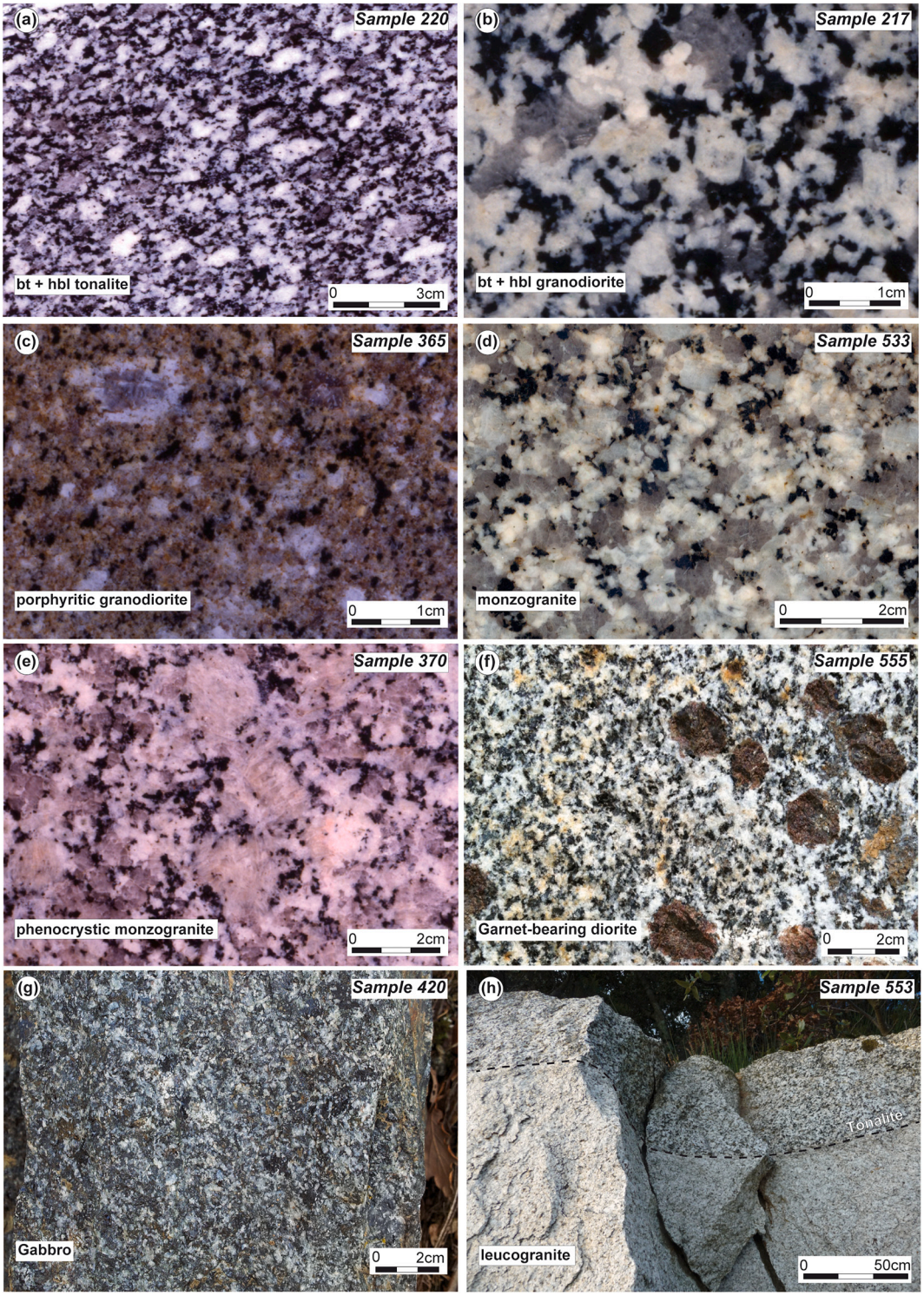

Fig. 2. Macroscopic aspect of the main studied rock types: (a) bt-hbl tonalite; (b) bt-hbl granodiorite; (c) porphyritic granodiorite; (d) monzogranite; (e) phenocrystic monzogranite from the SL-LJ pluton; (f) garnet-bearing diorite; (g) gabbro from the Ceret mafic complex; and (h) leucogranite dyke crosscutting the tonalite.

the granitoid, thus suggesting a pre-Triasic tilting of both the Roc de Frausa massif and the SL-LJ granitoid. D3 deformation event is related to the movement of oblique dextral-reversal shear zones. The parallelism of fold axial planes and direction of shear zones and most importantly, the continuation of these shear zones into damage zones of faults affecting Paleocene rocks above represent other structural criteria relating them to the Alpine cycle (Aguilar et al., 2015). The post-Variscan age obtained for the shear zones at the north-central part of the SL–LJ pluton using the $^{40}Ar—^{39}Ar$ method (El Pertús shear zone, ca. 48 Ma in biotite and feldspars, Soliva, 1992 and 38 Ma in phengitic white mica from an ultramylonitic rock; Maurel, 2003) corroborate this age, although the shear zones probably reactivate previous Variscan structures.

3. Field relationships

3.1. The calc-alkaline Sant Llorenç – La Jonquera pluton

The SL–LJ pluton is a large (~290 km^2 of currently exposed surface) sheet-like (~3.5 km thick) multiple intrusion elongated in an *E*-W direction, parallel to the Pyrenean trend. A complete section of the SL–LJ pluton —from the floor to the roof— crops out in the southern flank of the antiform, constituting the whole Roc de Frausa Massif (Aguilar et al., 2015; Liesa and Carreras, 1989). The floor lies above the lower levels of the Upper Proterozoic – Mid Ordovician sequence and it is concordant with the main lithological contacts and with the Variscan foliation (S1) of the country rocks. The roof of the intrusion is mostly eroded except for local exposures below the Upper Ordovician – Silurian metasediments (Fig. 1b). The contact is roughly parallel or has a gentle dip and minor stoped blocks are located beneath the roof. Maastrichtian-Danian rocks (Garumnian facies) unconformably overlie the granite and the pre-Variscan sequence. The eastern side of the pluton is steep and cross-cuts the Upper Proterozoic to Mid-Ordovician series of the L'Albera Massif (Vilà et al., 2005, 2007). To the west, the Ribes-Camprodon thrust-sheet is limited by the overlying Canigó Massif. In the northern flank of the antiform, the floor of the pluton steepens and cuts the deeper layers of the Roc de Frausa and L'Albera series. Based on these field relationships we can estimate the dimensions of the pluton: 3.5 km thick, similar to the 4 km thickness of the corresponding section of the L'Albera series occupying the same structural position of the pluton, as calculated by Vilà et al. (2005), with an outcropping area of approximately 290 km^2 in spite of the fact that part of the pluton lies below the Mesozoic metasediments, where it crops out as small units towards the south of the main outcrop.

The SL–LJ pluton exhibits distinctive petrographic zonation with tonalite – quartz diorite located at the base of the intrusion, granodiorite and minor monzogranite in the central part, and pink phenocrystic monzogranite towards the roof (Fig. 2a–e). The contact between the tonalite and the granodiorite is gradational. Towards the roof, the granodiorite has a porphyritic rapakivi texture at the intrusive contact with the monzogranite or with the chlorite-muscovite zone country rock (Fig. 2c). Phenocrystic monzogranite is clearly distinct from the other granitoids by the coarser grain size (2–3 mm), the presence of pink coloured euhedral K-feldspar phenocrysts (10 × 20 mm) (Fig. 2e), and miarolitic cavities.

The intrusion was emplaced during late D1 or early D2 as inferred from the magmatic fabric parallel to S1, the orientation of microgranular mafic enclaves, and the anisotropy of the magnetic susceptibility (Aguilar et al., 2015; Liesa, 1994; Olivier et al., 2016). In Fig. 1b, representative mineral lineation data from Olivier et al. (2016) are represented. These lineations have been folded by the D3 antiform, thus they dip to the southeast in the southern part of the SL–LJ pluton, are subhorizontal in the culmination area and dip steeply to the north in the northern part of the pluton. A contact aureole, approximately 500 m wide, is developed in the country rocks. Below the intrusive sheet, hornfelses with sillimanite – cordierite-bearing assemblages overprint medium-grade regional metamorphic rocks. At the top of the intrusion lower grade cordierite hornfelses and spotted phyllites overprint the biotite schists formed during the previous regional metamorphic event (Aguilar et al., 2015; Liesa and Carreras, 1989; Vilà et al., 2005).

Early dating attempts of the Sant Llorenç – La Jonquera pluton (Rb—Sr on whole rock) yielded an emplacement age of 282 ± 5 Ma (Cocherie, 1984). A tonalite sample from the base of the pluton was dated by Maurel (2003) at 301.7 ± 3.2 Ma ($^{40}Ar—^{39}Ar$ method on hornblende) and 295 ± 7 Ma (U—Pb FIB on zircon). Baudin et al. (2009) dated (U—Pb on zircon) a tonalite sample at 299 ± 6 Ma and a late granite from the upper part of the pluton crosscutting monzogranite at 304 ± 5 Ma. Denèle et al. (2012) reported ages between ca. 301 and 305 Ma from two tonalites and a granodiorite sample (U—Pb ID-TIMS on zircon). Aguilar et al. (2014) yielded significantly older ages from a tonalite sample using U—Pb SHRIMP-RG dating on zircon. According to the latter authors, the zircons display oscillatory zoning that is typical of magmatic environments with luminescent homogeneous cores that yield an age of 314.2 ± 1.5 Ma and a rim age of 311.0 ± 0.9 Ma. These authors interpreted the cores as antecrysts since the zircons display variable REE contents.

3.2. The Ceret and Mas Claret mafic complexes

Mafic complexes occur as sets of minor intrusions associated with the SL–LJ pluton. These are emplaced in the deeper crustal levels of the Upper Proterozoic – Mid Ordovician sequence (Fig. 1b), which is structurally below the SL–LJ intrusion. Individual mafic intrusions have small dimensions, between 1 and 10 km^2, round to elongated shapes on their surface and display a funnel shape at depth as deduced from their cross-sections (Liesa and Carreras, 1989). The Ceret mafic complex is the largest one and consists of a main intrusive body with associated m- to dm-scale satellite bodies scattered within a radius of ~2 km in the country rock (Fig. 1b). Mas Claret mafic complex is formed by five—currently separated— bodies cropping out at the northeastern margin of the SL–LJ granitoids, aligned in a NW-SE direction (Fig. 1b).

The mafic complexes mostly consist of amphibole-bearing gabbro, diorite, and tonalite, with minor proportions of ultramafic cumulates. Diorite is the most abundant rock type in the Ceret mafic complex, whereas gabbro dominates in the Mas Claret mafic complex. Garnet-bearing diorite or gabbro locally occurs next to the contact with the metapelitic country rock (Fig. 2f). No contacts are recognized between the dioritic and gabbroic varieties. Ultramafic cumulates (hornblendite and/or cortlandite) occur as decametric irregular bodies within the diorite/gabbro. They are mostly weathered to a black coarse sand cm-mm in grain size with no clear contacts observed. When the degree of weathering is lower, the rock texture is preserved, although alteration of the minerals is strong. A number of xenoliths of the country rock are included inside the mafic complexes. They typically have rounded to elliptical shapes making diffuse contacts with the hosting igneous rocks, and they can be dismembered (Aguilar et al., 2016).

Field relations indicate that the mafic complexes were emplaced coeval to the D2 event (Aguilar et al., 2015). U—Pb SHRIMP-RG zircon analysis of the Ceret gabbro revealed two magmatic pulses in one single sample: an early one at ca. 312 Ma corresponding to a more evolved magma and a late one at ca. 307 Ma corresponding to a less evolved magma (Aguilar et al., 2014).

Metapelites that form xenoliths or which reside in the inner contact metamorphic aureole (~ 250 m width) are partially melted and present migmatitic textures. These migmatites contain the assemblage garnet + cordierite + biotite + sillimanite + K-feldspar + quartz + plagioclase in the melanosome as well as in the leucosome quartz + plagioclase + K-feldspar +/− garnet/cordierite/biotite. Detailed description of the migmatites is given in Vilà et al. (2007) and Aguilar et al. (2016). Aguilar et al. (2016) estimated *P–T* conditions in the range of ~0.7–0.8 GPa to ~0.5 GPa at temperatures between ~840 °C and 690 °C, which represent the metamorphic climax of the country rocks and therefore constrain the conditions at which the mafic rocks may have intruded.

3.3. Leucogranite

Leucogranite occurs as numerous irregular leucosomes in the metamorphic rock (anatectic leucogranite) or as bodies or dykes that intrude the SL–LJ pluton, the mafic complexes, and the metasedimentary country rock. Anatectic leucogranite forms numerous irregular bodies, mostly in the migmatite zone, from cm-scale leucosomes to km-scale leucogranite stocks, thus suggesting the coalescence of leucosomes to form larger bodies. They are dominated by quartz, plagioclase, and less abundant K-feldspar. Muscovite can also be present in the lower grade leucosomes and migmatites. The bodies or dykes of leucogranite, which intrude into the SL–LJ pluton have hectometric to kilometric extension and are generally elongated NE-SW. The biggest leucogranite body (El Castellar leucogranite, more than 8 km^2) forms a peripheral intrusion east of SL–LJ, cutting the whole metamorphic series (Fig. 1b). It crops out as an elongated NW-SE pluton intruding the migmatitic metasediments towards the N and the progressively lower grade rocks towards the south. The contact between leucogranite bodies and SL–LJ pluton, the mafic rocks, or the metasediments varies according to the structural level to which it intrudes. At its northern end, where the higher metamorphic grade rocks and the deeper levels of the SL–LJ pluton crop out, it is diffuse and the leucogranite contains numerous xenoliths of metasediments. When the leucogranite intrudes the central part of the SL–LJ pluton, the mafic rocks, or the lower grade metamorphic rocks, it forms sharp boundaries and locally shows textural banding parallel to the contact (Fig. 2h). These field relations indicate that leucogranites are the last intrusive episode that took place during *syn*-late-D2.

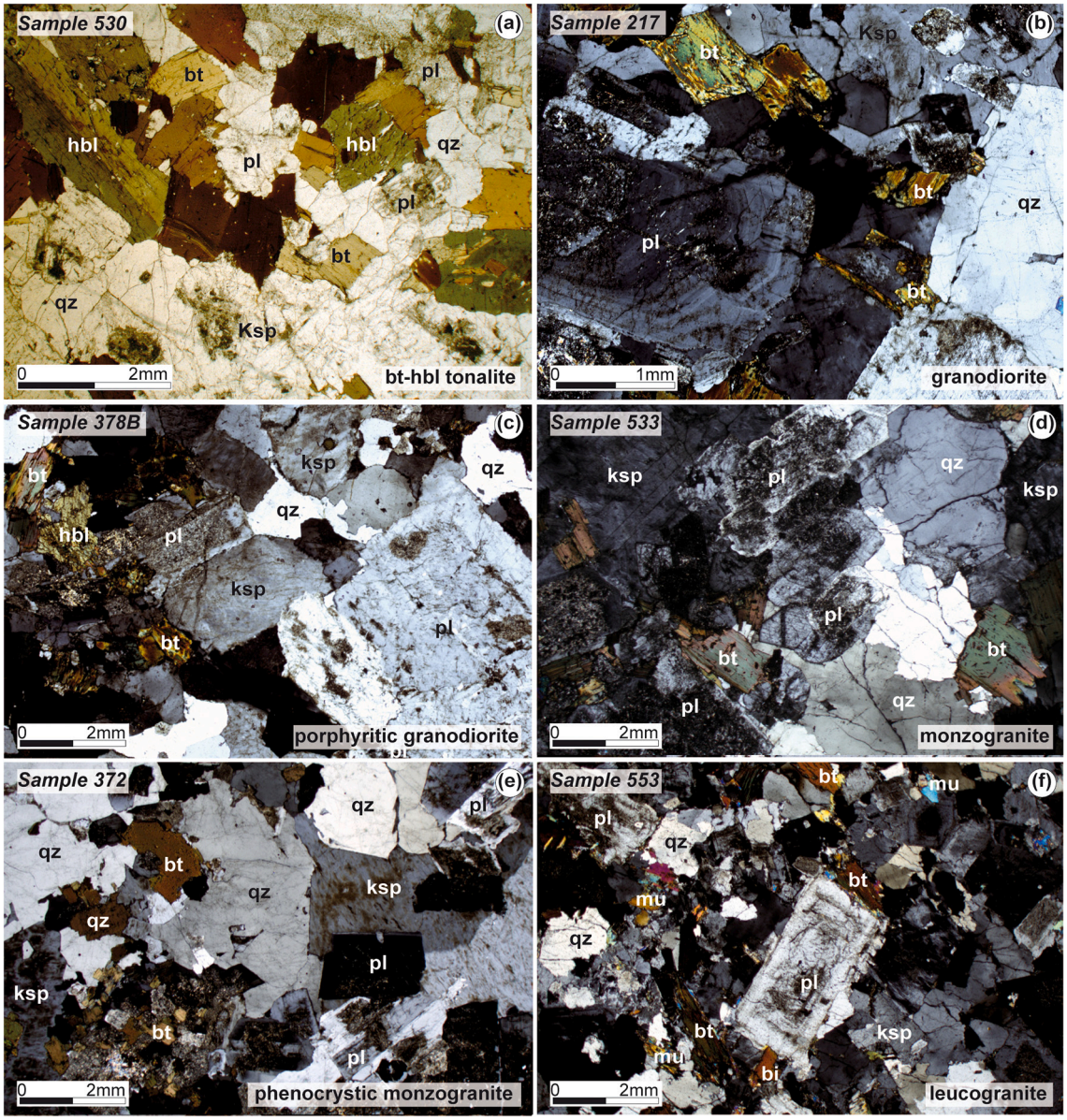

Fig. 3. Microscopic aspect of the main rock types from the SL–LJ pluton: (a) biotite and hornblende crystallizing in clusters in the tonalite; (b) zoned plagioclase phenocryst (up to 4 mm), biotite and poikilitic K-feldspar including quartz in the granodiorite; (c) porphyritic granodiorite with a plagioclase phenocryst and a matrix formed by hornblende and biotite clusters, K-feldspar and interstitial quartz; (d) inequigranular monzogranite with K-feldspar partially mantling plagioclase, rounded quartz aggregates and small biotite; (e) monzogranite with twinned phenocryst of K-feldspar (pink in hand-sample, Fig. 2e), subhedral-anhedral quartz and scarce biotite and plagioclase; and (f) euhedral plagioclase in an inequigranular muscovite-biotite leucogranite with post-crystalline deformation. Mineral abbreviations follow Whitney and Evans (2010): hbl, hornblende; gru, grunerite; cpx, clinopyroxene; qz, quartz; pl, plagioclase; ksp, K-feldspar; grt, garnet; bt, biotite; mu, muscovite; ol, olivine; chl, chlorite. (For interpretation of the references to colour in this figure legend, the reader is referred to the web version of this article.)

4. Petrography

4.1. The calc-alkaline Sant Llorenç – La Jonquera pluton

4.1.1. Tonalite – quartz diorite

Tonalite is formed by plagioclase, biotite, hornblende, interstitial K-feldspar, and quartz, though hornblende can be locally absent (Fig. 2a). The modal content of quartz can decrease to less than 20% in certain areas, and the rock is locally classified as quartz diorite. It has a granular texture with a preferred orientation of stubby prisms of plagioclase and elongate grains of biotite and euhedral hornblende (Fig. 3a). Biotite and hornblende crystallize in aggregates and biotite can be included in the hornblende. Biotite contains a large number of zircon and apatite inclusions. Hornblende is zoned, and is lighter-coloured in the core than in at its rim. Plagioclase displays oscillatory zoning (An 18–50). K-feldspar is interstitial and has an irregular distribution. Locally it forms myrmekites with plagioclase. Opaque phases and allanite (up to 10 mm) are other accessory minerals. Alteration minerals are clinozoisite, epidote and sericite from plagioclase, in addition to chlorite from biotite. It presents microgranular enclaves of quartz diorite composed of plagioclase, quartz, biotite, and hornblende. They are fine grained (< 1 mm), although plagioclase can be bigger than the other minerals. They can develop a leucocratic halo in contact with the tonalite.

4.1.2. Granodiorite and porphyritic granodiorite

Granodiorite is texturally similar to tonalite although it is characterized by a lower content of biotite and hornblende (Figs. 2b-c, 3b-c) or null hornblende. K-feldspar is poikilitic and includes plagioclase, biotite, and hornblende. Quartz content is slightly higher than that of tonalite and it can be correlated with a minor abundance of mafic minerals. The granodiorite in the border facies against the monzogranite has a porphyritic rapakivi texture given by pink K-feldspar (1 cm) mantled by a rim of white plagioclase (1–2 mm, Fig. 2c) which is embedded in a finer-grained quartz-feldspathic groundmass.

4.1.3. Monzogranite and phenocrystic monzogranite

Two main facies of monzogranite crop out, mostly characterized by the textural aspect of K-feldspar (Fig. 2d, e). Monzogranite has idiomorphic plagioclase and interstitial K-feldspar, with biotite as its only mafic phase (Fig. 3d). It has coarse quartz which forms rounded aggregates of around 6 mm and smaller feldspar and biotite (around 2 mm). Plagioclase tends to be idiomorphic and slightly zoned. A distinctive facies of phenocrystic monzogranite crops out mostly at the south and west of the SL–LJ pluton. It consists of pink coloured euhedral K-feldspar phenocrysts (10 × 20 mm) with Carlsbad twinning embedded in a coarse-grained matrix (2–3 mm) (Fig. 2e). The matrix is formed by quartz, plagioclase, K-feldspar and scarce biotite. Quartz locally develops crystalline faces (Fig. 3e). Towards the roof of the intrusion K-feldspar becomes anhedral and the granite presents miarolitic cavities.

4.2. The Ceret and Mas Claret mafic complexes

4.2.1. Diorite

Diorite has a granular texture and a grain size between 1 and 3 mm (Figs. 2f, 4a, b). It contains plagioclase (> 50 modal %), biotite (2–20 modal %), and interstitial quartz (5–10 modal %) as its main mineral phases, and opaque minerals (mostly ilmenite), apatite, and zircon as its accessory phases. It generally contains amphibole (up to 35 modal %)

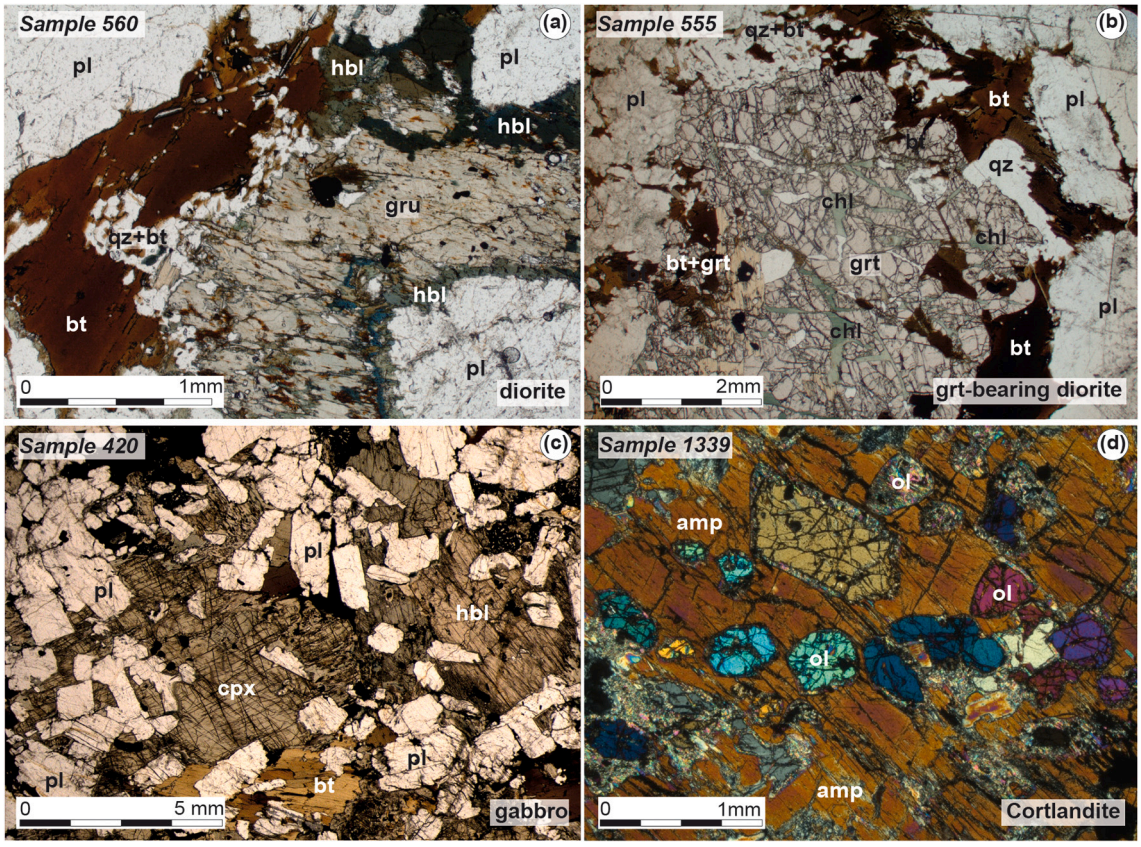

Fig. 4. Microscopic aspect of the main mafic-ultramafic rocks: (a) detail of a diorite with grunerite aisled from plagioclase by a rim of hornblende and from biotite by a symplectite of quartz + biotite; (b) detail of a corroded garnet in contact with plagioclase and partially pseudomorphed by biotite in a garnet-bearing diorite; (c) ophitic texture in a gabbro with poikilitic clinopyroxene including idiomorphic plagioclase. Hornblende and biotite are also part of the assemblage; and (d) cortlandite with large greenish-brown (in polarized light) poikilitic amphibole including subhedral crystals of olivine. Mineral abbreviations in Fig. 3. (For interpretation of the references to colour in this figure legend, the reader is referred to the web version of this article.)

together with biotite, although their content is negatively correlated. Near the contact with the metapelitic country rock, diorite may contain large garnet crystals (up to 40 mm diameter) (Figs. 2f, 4b). Plagioclase forms large laths (up to 3 mm) and is poorly zoned. It is partially altered to sericite. Biotite is subhedral, with a tabular habit and occupies interstices between the plagioclase and the amphibole (Fig. 4a). It grows as isolated crystals or in clots with amphibole. In some diorite samples, it forms big poikilitic laths with amphibole or plagioclase inclusions, and it is locally altered to chlorite. Quartz is anhedral and occupies the interstices between minerals. Two types of amphiboles are distinguished: a pale green to bluish grunerite with a transparent core and weak pleochroism, as well as dark green to brown prismatic-fibrous hornblende (see 6.1. for amphibole classification). Grunerite forms either single crystals or polycrystalline aggregates (clots). It is generally mantled by hornblende (Fig. 4a) and both phases can be in optical and structural continuity, although hornblende can also form isolated crystals. Grunerite is in contact with plagioclase or garnet, whereas hornblende is not in textural equilibrium with garnet. Garnet occurs as euhedral to anhedral equidimensional fractured crystals with chlorite filling the fractures. Locally, garnet has a leucocratic halo consisting of plagioclase with minor biotite and quartz, which also fills garnet embayments. Under the microscope, biotite abounds as inclusions within garnet crystals near the rim, as well as surrounding it (Fig. 4b).

4.2.2. Gabbro

Gabbro consists of plagioclase (20–60 modal %) and amphibole (20–75 modal %) as the main phases, among pyroxene, biotite, minor olivine, and interstitial quartz (Fig. 4c). Apatite, ilmenite, zircon, and titanite are common accessory minerals. The texture grades from ophitic with idiomorphic plagioclase laths enclosed in amphibole or pyroxene, to intergranular with mafic minerals occupying plagioclase interstices. Plagioclase is zoned and it is locally altered to epidote in the core. Biotite is xenomorphic and it can intergrow with amphibole. As with the diorite, two types of amphiboles are present: dark green to brown hornblende and a less abundant pale green to bluish grunerite which is locally mantled by hornblende (Fig. 4c). Biotite and amphibole include olivine, clinopyroxene or orthopyroxene and may form a coronitic texture around them. Orthopyroxene can also be included in plagioclase. Large garnet (up to 2 cm in diameter) is locally present close to the contact with the metapelites or migmatites. It is corroded and surrounded by a quartz-feldspar halo with minor biotite and amphibole, as in the garnet-bearing diorite.

4.2.3. Ultramafic cumulates

Only one sample collected from the Ceret mafic complex and a few samples from the Mas Claret mafic complex are fresh enough to be petrographically described (Fig. 4d). Ultramafic rocks have a coarse-grained granular to poikilitic texture with relatively fresh brown amphibole, olivine, and orthopyroxene. Amphibole oikocrysts have an elongated subhedral to anhedral shape with a shorter axis around 5–10 mm. In thin section they are mostly dark green to brown (pargasite, hornblende or cummingtonite). When zoned, cores are lighter and have a thin peripheral alteration to chlorite. Amphibole fills interstices or has a poikilitic texture that includes olivine and orthopyroxene (Fig. 4d). Olivine (Fo 75–79) occurs as euhedral to subhedral or amoeboid crystals (0.2–1 mm) that are partially to completely altered to serpentine (Vilà et al., 2005). Orthopyroxene (En 80–84) forms euhedral crystals with a rectangular shape of around 8 × 5 mm. It can have corroded rims in contact with the amphibole. Biotite occurs in interstices. The rocks are dotted and veined by a secondary opaque iron-bearing mineral (magnetite), forming rounded to elongated aggregates, which fill the cracks.

4.3. Leucogranite

Leucogranite consists of quartz, perthitic K-feldspar (orthoclase or microcline), plagioclase (An26 core —› An 10 rim), and scarce biotite plus/minus muscovite or occasionally cordierite, garnet, or sillimanite (Figs. 2h, 3f). Tourmaline, apatite, and zircon are the main accessory minerals. Its microstructure varies from granular to aplitic (1 mm) or, locally, pegmatitic (up to 20 mm). K-feldspar forms euhedral phenocrysts (up to 50 mm), quartz is euhedral to subhedral and plagioclase forms zoned euhedral crystals. The two micas can form aggregates or crystallize in subhedral isolated crystals.

5. Whole-rock geochemistry and Sr—Nd isotopic ratios

The geochemical study includes 55 new whole-rock analyses of major and trace elements of SL–LJ granitoids, the Mas Claret and Ceret mafic complexes, and leucogranites. Details of the methodology can be found in the Supplementary Material (Appendix A.1). The results of the analyses are presented in Figs. 5 to 9 and in Tables S1 to S5 of the Supplementary Material. For the Ceret mafic complex two separate rock populations are distinguished according to their Zr content: high-Zr (1250–2000 ppm) and regular-Zr (125–300 ppm) (Fig. 5a). These two groups are assigned different symbols in the diagrams and are described separately in the following sections. In addition, 13 new orthogneiss analyses, together with 50 published analyses of the country rocks (3 orthogneisses, 13 metapelites, and 35 migmatites from Vilà et al., 2005, 2007 and Aguilar et al., 2015, 2016), are also plotted in order to assess the likely effects of their assimilation into the magmas. An igneous dataset was compiled, which included 48 published analyses from the SL–LJ pluton, the Mas Claret mafic complex and the leucogranites, in addition to around 600 analyses from other granitic plutons and mafic-associated rocks of the Pyrenees and Catalan Coastal Ranges to compare with our data. The analyses from the SL–LJ pluton, the Mas Claret mafic complex and the leucogranites are from Cocherie (1984) and Vilà et al. (2005, 2007) and are plotted in the figures with their corresponding symbol, but with a smaller size. The data from the Pyrenees and Catalan Coastal Ranges are drawn in grey colour in all figures and the sources are indicated in the Supplementary Material (Appendix A.1).

Moreover, 24 new analyses of Sr—Nd whole-rock isotope ratios of SL–LJ granitoids, mafic rocks, leucogranites, and country rocks (orthogneiss, metapelites, and migmatites) are also included (Fig. 10 and Table S6 of the Supplementary Material) as measured, and with age-corrected values following Faure and Mensing (2005). Details of methodology can be found in the Supplementary Material (Appendix A.1). The isotopic data are supplemented with published values of samples from the eastern part of the SL–LJ pluton, the Mas Claret mafic complex and the leucogranites, as well as metapelites, migmatites, and orthogneisses from the L'Albera Massif (Vilà et al., 2005).

5.1. Major elements

Rocks from the Ceret and Mas Claret mafic complexes (gabbro to diorite) range in SiO_2 content from 49 to 57 wt%, SL–LJ granitoids (tonalite to monzongranite) have 57–77 wt% SiO_2 and the leucogranites range from 67 to 77 wt% SiO_2 (Fig. 5b-h). They all form a continuum in the silica space, although there is a lower number of rocks with compositions between 57 and 61 wt% SiO_2. Ultramafic cumulates have SiO_2 around 42 wt% and MgO > 10 wt% and have not been represented in the diagrams according to the filter used in the data (see detail in Appendix A.1 of Supplementary Material).

In Harker diagrams (Fig. 5b-h), major elements show a strong correlation with silica for SL–LJ granitoids and consistent linear trends for most elements of the mafic rocks and leucogranites, although a larger dispersion is seen for some elements in the mafic rocks (e.g., Al_2O_3, TiO_2, and MgO) and leucogranites (e.g., Na_2O, K_2O). For the three groups of rocks, Al_2O_3, TiO_2, FeOt, MgO, and CaO define decreasing trends alongside increasing SiO_2 with a slightly concave trend for MgO. The Na_2O trend is approximately horizontal, mostly for SL–LJ granitoids. K_2O shows a positive correlation with SiO_2 showing dispersion in the

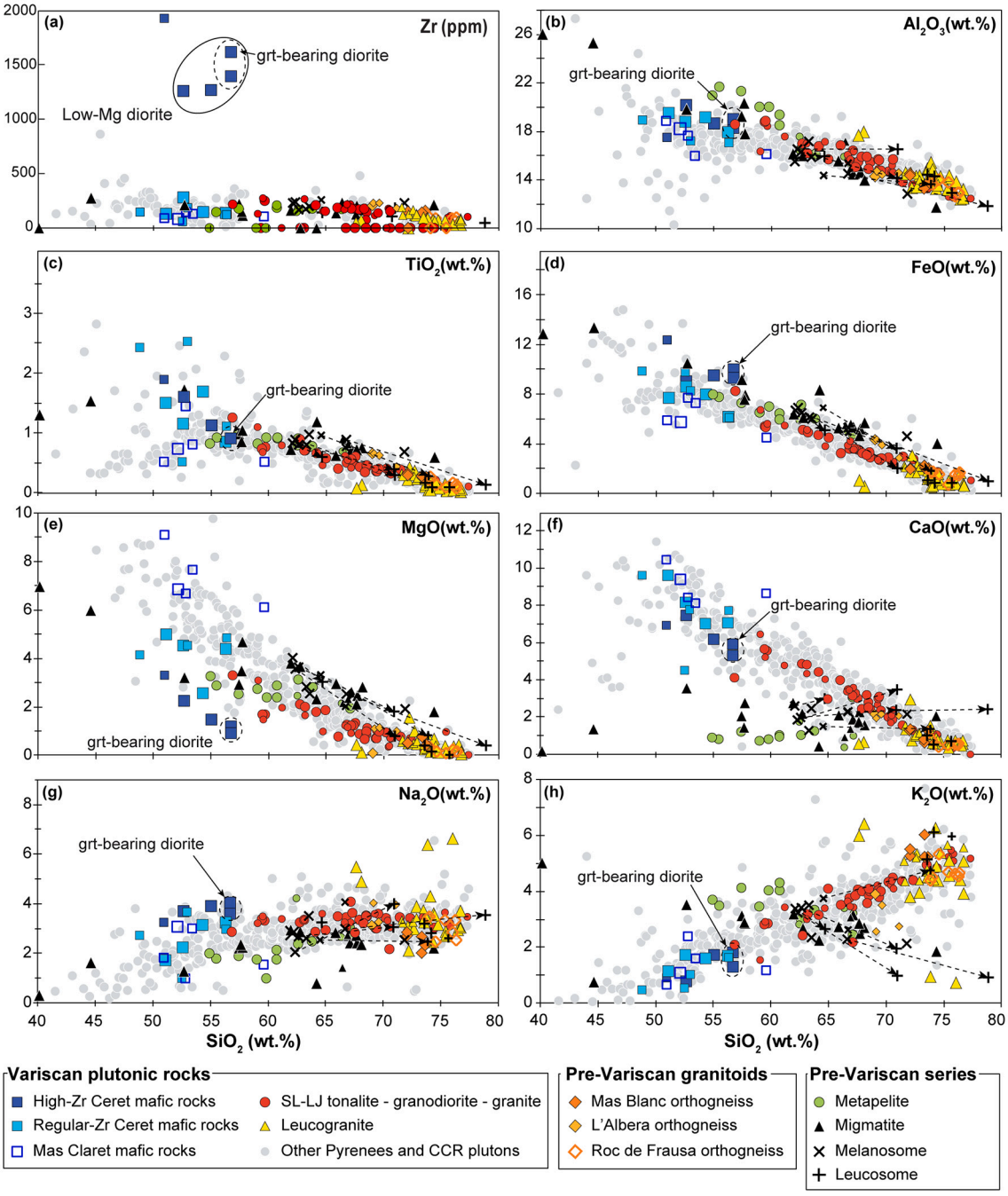

Fig. 5. Harker plots of the studied samples. (a) SiO_2 (wt%) versus Zr (ppm); (b-h) SiO_2 versus major elements (Al_2O_3, TiO_2, FeOt, MgO, CaO, Na_2O, and K_2O) in wt%.

leucogranite samples. Within these general trends, rock populations of the mafic complexes depict three separate subparallel trends. For instance, Mas Claret mafic rocks present low Al_2O_3, TiO_2, and FeOt, with high MgO and CaO, whereas high-Zr Ceret mafic rocks show opposite values and regular-Zr Ceret rocks are in between (Fig. 5b-h). The trends defined by regular-Zr Ceret mafic rocks are roughly aligned with those from the SL–LJ pluton. The largest difference between trends is in their MgO contents, with a range from 2 (high-Zr Ceret) to 7.5 (Mas Claret) wt % at 55 wt% SiO_2. For this element, the low-MgO in high-Zr Ceret mafic rocks falls below the field defined by rocks from the Pyrenees and Catalan Coastal Ranges (Fig. 5b-h) but, as a whole, the observed compositions are consistent with the existing geochemical database of Variscan igneous rocks from the Pyrenees and Catalan Coastal Ranges. Orthogneisses present heavily differentiated compositions, similar to those of leucogranites for all major elements. Metapelites and migmatites fall outside the differentiation patterns of Variscan igneous rocks, especially for CaO and K_2O.

The studied rocks are depicted in Frost et al. (2001) chemical discrimination diagrams (Fig. 6). In the Fe* (FeOt/FeOt+MgO) versus SiO_2 diagram (Fig. 6a), most Variscan igneous rocks classify as magnesian according to the empirical division line of Miyashiro (1970). In contrast, high-Zr Ceret mafic complex rocks, the most differentiated SL–LJ granitoids, in addition to some leucogranites, are depicted in the ferroan field. For the high-Zr mafic rocks, the significantly higher Fe* is the consequence of their low MgO (< 3 wt%) and slightly higher FeOt content (4–12 wt%). Pre-Variscan metapelitic country rocks are magnesian, whereas orthogneisses can be either ferroan or magnesian (Fig. 6a). Altogether, SL–LJ granitoids and mafic rocks share a common

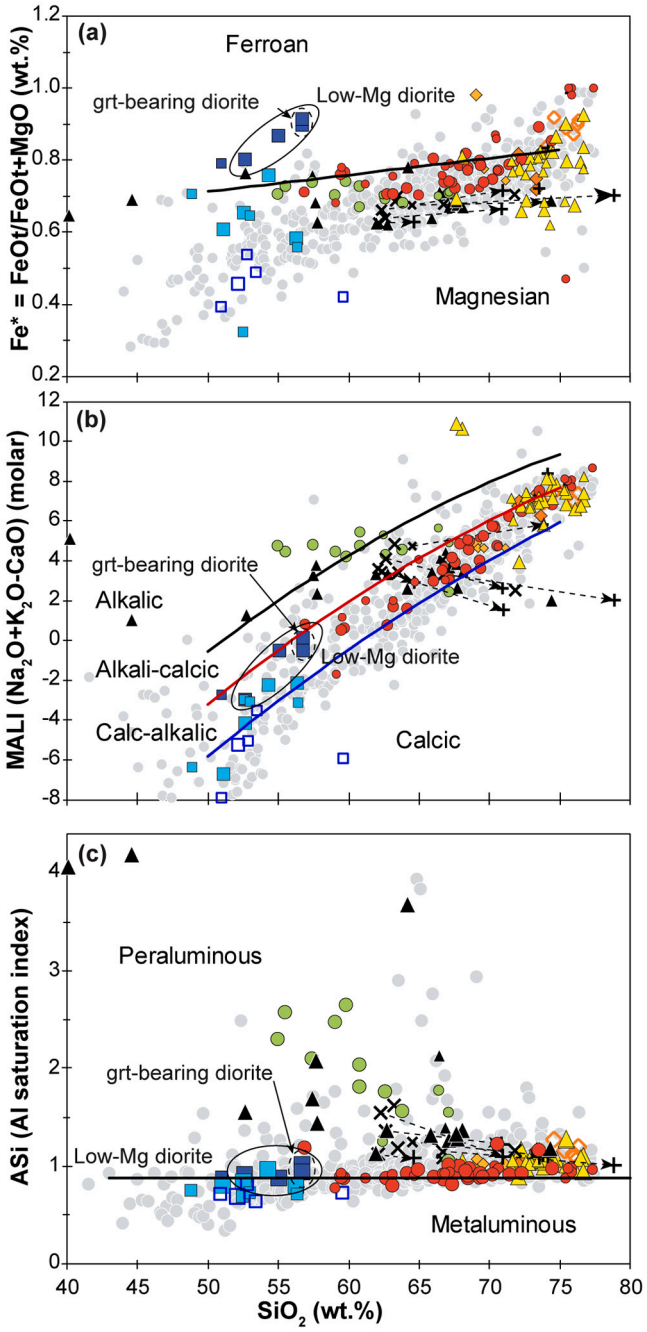

Fig. 6. Chemical discrimination diagrams of the studied samples after Frost et al. (2001) showing: (a) the mostly magnesian affinity; (b) the calc-alkaline trend; and (c) the peraluminous character (molar Al-saturation index ASI: $Al_2O_3/Na_2O + K_2O + CaO - 3.3P_2O_5$). Symbol legend in Fig. 5.

Peacock index following values close to the calc-alkalic trend (Fig. 6b). Two regular-Zr Ceret and most of the Mas Claret mafic rocks show a lower index and are represented in the calcic field. Leucogranites mostly fall within the calc-alkalic and alkali-calcic fields. Metapelites and migmatites fall in the alkali-calcic and alkalic fields. In the ASI diagram (Fig. 6c), most of Mas Claret and regular-Zr Ceret mafic rocks are metaluminous with ASI values between 0.7 and 1, whereas high-Zr mafic rocks and SL–LJ calc-alkaline granitoids are predominantly slightly peraluminous with ASI values between 1 and 1.2. Leucogranites and orthogneisses are peraluminous and show a larger ASI range reaching up to 1.4. As expected, all metapelites and migmatites present peraluminous compositions.

Fig. 7a depicts a CaO vs MgO diagram with a clear linear trend for granitic and intermediate plutonic rocks and orthogneisses, and a major dispersion for mafic rocks. The granitoids, leucogranites, and orthogneisses are well grouped along a curved trend of cotectic liquids in agreement with plutonic rocks from the Pyrenees and Catalan Coastal Ranges, as well as with experimental melt compositions in calc-alkaline systems (black dashed line according to data in Castro, 2013, 2021). In contrast, Mas Claret mafic rocks are MgO rich and fall within the overall trend, whereas Ceret mafic rocks are represented above the trend, with lower MgO contents. Metapelites and migmatites have lower CaO and higher MgO compared to Variscan granitoids.

In the Mg# (MgO/MgO + FeO) versus B ((Fe + Mg + Ti)*1000) diagram (Fig. 7b), an overall positive correlation is shown. SL–LJ granitoids and regular-Zr Ceret mafic rocks broadly follow a typical calc-alkaline differentiation trend (dashed line) towards lower Mg# and B. High-Zr Ceret mafic rocks depart from the main trend, likely because of their significantly lower MgO content. Conversely, Mas Claret mafic rocks show a higher Mg#. Leucogranites show a large Mg# dispersion.

In the A ((Al-Na-K-2*Ca)*1000) vs B ((Fe + Mg + Ti)*1000) diagram (Fig. 7c), the three suites of Variscan plutonic rocks follow a regular trend of increasing aluminosity (A) with increasing fractionation (decreasing B) that is characteristic of the calc-alkaline (cafemic) trend. Mafic rocks fall into the metaluminous domain, SL–LJ rocks transit from metaluminous to slightly peraluminous, with samples on both sides of the A = 0 line; and leucogranites and orthogneisses are peraluminous. Pyrenees and Catalan Coastal Ranges granitoids and mafic rocks behave similarly and depict an overall typical calc-alkaline differentiation trend. Metapelites and migmatites do not follow the trend and fall within the peraluminous field.

In the F–An–Or diagram (Fig. 7d), mafic and SL–LJ rocks are located in the field of magma crystallization and fractionation that is characteristic of calc-alkaline trends (green line in Fig. 7d), consistently with previous diagrams. Leucogranites and orthogneisses are represented in the area of anatectic liquids. Some rocks from the SL–LJ pluton and the L'Albera orthogneiss depart from the typical cotectic trends (green and black dashed lines) and are located below the dashed line pointing to the composition of migmatites. Metapelites and migmatites are clearly discriminated and follow a trend of constant F/Or ratio in between anatectic melts (granite-nebulite trend) and restites.

5.2. Trace elements

In chondrite-normalized multielemental diagrams (Fig. 8) Variscan plutonic rocks show enrichment in LREE with respect to HREE, and Eu anomalies. Ceret and Mas Claret mafic rocks show a concave to flat profile of the HREE (one of the garnet-bearing diorites has a positive slope for HREE) and slightly negative to moderately positive Eu anomalies (Fig. 8a). Rocks from the SL–LJ pluton have a slightly higher enrichment in LREE than mafic rocks and leucogranites, a marked Eu depletion, and a flat HREE pattern (Fig. 8b). Leucogranites show lower REE content and, in all cases, a much wider range than SL–LJ granitoids and mafic rocks (Fig. 8c). REE patterns of leucogranites are less regular than those of the other Variscan igneous rocks and have moderately negative to moderately positive Eu anomalies. REE patterns of orthogneisses are similar to those of SL–LJ granitoids, but they display a wider compositional range at lower REE concentrations and HREE patterns from flat to increasingly depleted towards the heaviest REE (Fig. 8c). Metapelites and migmatites form a compact low variability group enriched in LREE and impoverished in HREE, with slight Eu depletion (Fig. 8d).

In primitive mantle-normalized trace element diagrams (Fig. 8e,f,g,h), analyzed rocks from the SL–LJ pluton, mafic complexes, leucogranites and orthogneisses display enrichment in LILE (e.g., Pb, Rb, K) relative to HFSE (e.g., Nb), being less pronounced for mafic rocks. Mafic magma trends depart from common calc-alkaline ones. Leucogranites present similar patterns to those of granitoids but with marked depletion

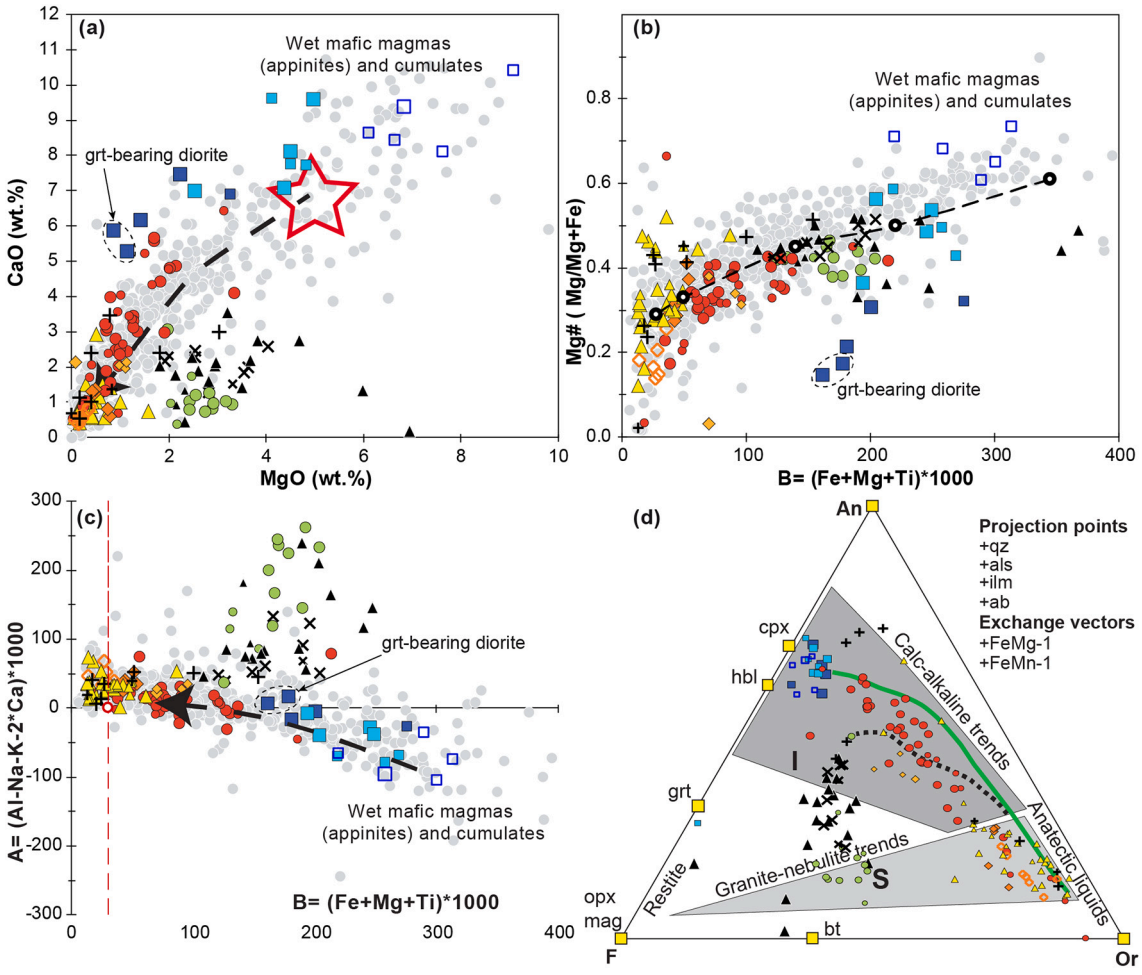

Fig. 7. Variation diagrams showing relations between relevant major elements of the studied samples. (a) CaO/MgO variation diagram. The curved line follows a path of cotectic liquids of calc-alkaline evolutionary trends in agreement with experimental data from Castro (2013). (b) Mg# versus B diagram (in milications 10^3 g-at.) (Debon and Le Fort, 1988); (c) A–B diagram (in milications 10^3 g-at.) (Debon and Le Fort, 1983); and (d) Pseudoternary projection into the compositional space Anorthite (An) F – (FeO + MgO + MnO) – Orthoclase (Or). Grey areas represent the fields of S- and I-type granitoids. Experimental cotectic lines from Castro (2013): dashed black line for initial water content 2.3 wt% and $P = 0.7$ GPa, and green line for initial water content 0.9 wt% and $P = 0.3$ GPa. Characteristic minerals are plotted for reference. Symbol legend in Fig. 5. (For interpretation of the references to colour in this figure legend, the reader is referred to the web version of this article.)

of REE, especially LREE (e.g., La, Ce). In addition, granitoids and orthogneisses have marked depletions in Ba and Sr and the high-Zr rocks of the Ceret mafic complex show a pronounced positive Zr anomaly. Metapelites have trace element patterns similar to those of granitoids and orthogneisses.

Fig. 9 shows trace element ratios of petrogenetic significance versus silica and Y. The Th/Nb ratio (Fig. 9a) of Ceret mafic rocks is nearly constant with increasing SiO_2, in contrast to the corresponding ratio from Mas Claret mafic rocks, which increases from 1 to 2 as a function of the differentiation degree. The Th/Nb ratio of SL–LJ granitoids is higher than that of Ceret mafic rocks at low SiO_2 values and it increases slightly with differentiation except for anomalously high values for two samples at the high-silica end. Leucogranites and orthogneisses show a highly variable Th/Nb ratio, with values ranging from nearly 0 to 9. The Th/Nb ratio of metapelites and migmatites is similar to that of granitoids. The Nb/Zr and Nb/Y ratios (Fig. 9b, c) are nearly constant for all igneous rocks except leucogranites and orthogneisses. For both the plutonic rocks and the country rocks, the Nb/Zr ratio is lower than 0.1 and the Nb/Y ratio is <1. In contrast, leucogranites and orthogneisses show a wider compositional range towards higher SiO_2 values (up to 0.3 Nb/Zr and 5.5 Nb/Y). In the bivariate plot of Sr/Y versus Y (Fig. 9d), igneous rocks show a negative correlation within each individual rock group. SL–LJ granitoids and leucogranites mostly show a low Sr/Y ratio, whereas mafic rocks including the two garnet-bearing diorites have a much higher Sr/Y ratio for low Y contents.

5.3. Sr—Nd isotopic ratios

The samples analyzed in this study were corrected to 300 Ma (average emplacement age of Variscan plutonic rocks based on Aguilar et al. (2014); Fig. 10). The rock populations studied in this work have clearly distinct isotope compositions, depicted in the ε_{Nd} versus $^{87}Sr/^{86}Sr$ at 300 Ma diagram (Fig. 10). The most mafic-ultramafic population —that of Mas Claret mafic complex— has the most radiogenic Nd and the least radiogenic Sr, with $\varepsilon_{Nd} = -3.0$–0.7 and $^{87}Sr/^{86}Sr = 0.703774$–$0.706449$. Ceret mafic rocks present lower Nd and higher Sr isotope ratios ($\varepsilon_{Nd} = -8.1$ to -6.1 and $^{87}Sr/^{86}Sr = 0.709541$–$0.711848$) regardless of their regular- or high-Zr character. Ceret mafic rocks have lower Nd isotope ratios than SL–LJ granitoids, which present a narrow isotope composition for the whole petrologic range ($\varepsilon_{Nd} = -6.9$ to -5.6 and $^{87}Sr/^{86}Sr = 0.709695$–$0.712705$). Leucogranites have a wide compositional variability. Most samples are in the $^{87}Sr/^{86}Sr$ range of 0.716047–0.721750, similar to that of the metapelites and the less radiogenic L'Albera orthogneisses and only one leucogranite sample has

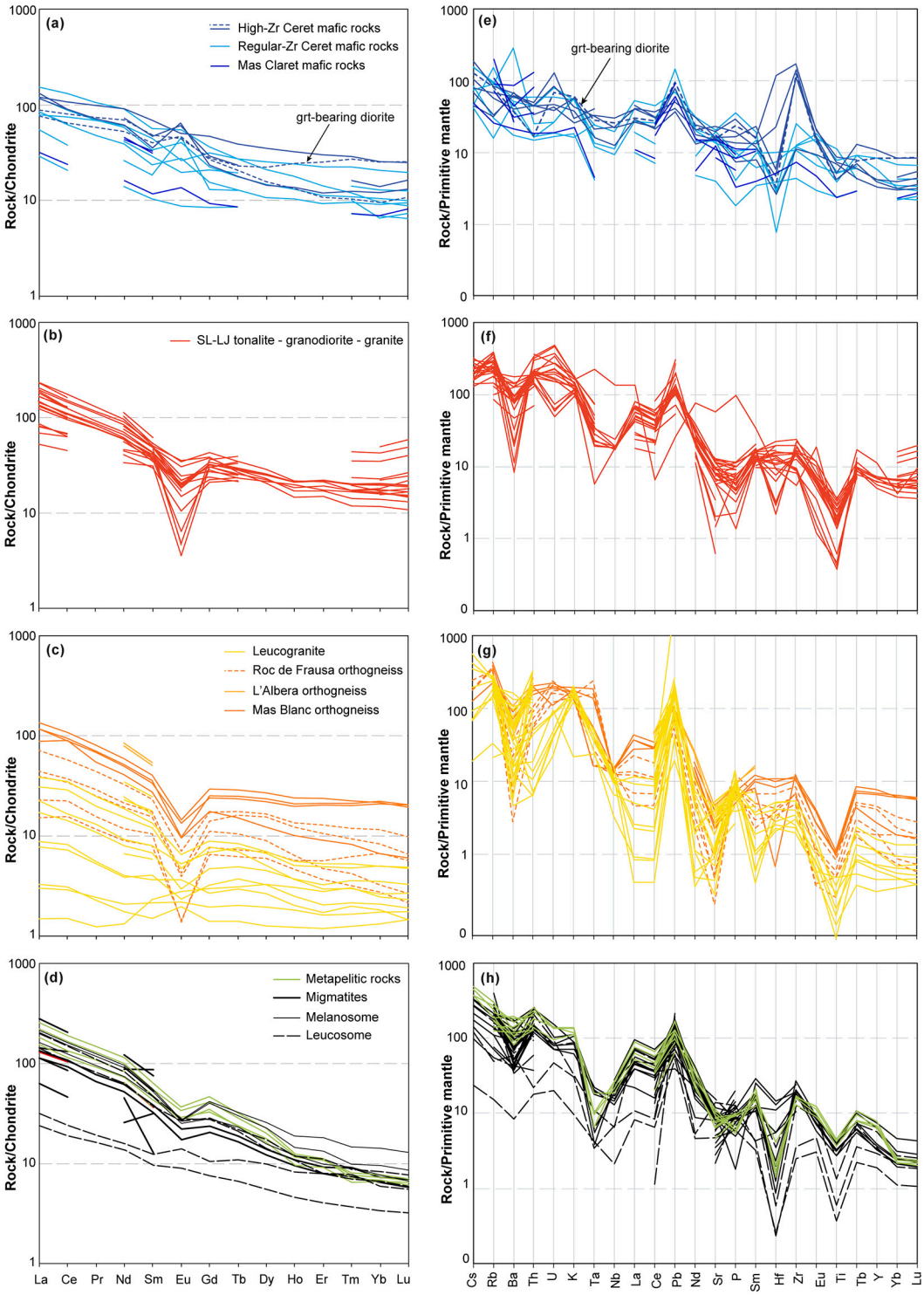

Fig. 8. Average chondrite-normalized REE patterns (a, b, c, d) (Evensen et al., 1978) and primitive mantle-normalized extended trace element spider patterns (e, f, g, h) (Sun and McDonough, 1989) for the rocks from the Ceret and Mas Claret mafic complexes, SL–LJ pluton, leucogranites and orthogneisses, metapelites and migmatites.

a more radiogenic $^{87}Sr/^{86}Sr = 0.746510$. The ε_{Nd} of leucogranites is similar to that of SL–LJ granitoids and Ceret mafic rocks, in between the orthogneisses and the dominant values for metapelites and migmatites (−7.5 to −5), except for the high-$^{87}Sr/^{86}Sr$ sample, which has a highly radiogenic ε_{Nd} of −2.4. At 300 Ma orthogneisses present a narrow Nd isotopic compositional range, equivalent to that of the SL–LJ granitoids but a much higher Sr isotopic range ($\varepsilon_{Nd} = -6.4$ to −4.6 and $^{87}Sr/^{86}Sr = 0.718533–0.754623$). Metapelites and migmatites cover a large compositional range ($\varepsilon_{Nd} = -15$ to −4.5 and $^{87}Sr/^{86}Sr = 0.704952–0.722565$) although two separate populations can be recognized: 1) a main low-ε_{Nd} one represented by most regional and contact metamorphic migmatites ($\varepsilon_{Nd} = -15$ to −9.5 and $^{87}Sr/^{86}Sr = 0.712919–0.722565$), which presents the least radiogenic Nd compositions of all studied rocks; and 2) a minor high-ε_{Nd} one ($\varepsilon_{Nd} = -6.3$ to −4.5 and $^{87}Sr/^{86}Sr = 0.704952–0.712686$). Except for the Mas Claret mafic rocks, all analyzed rock populations fall within the compositional

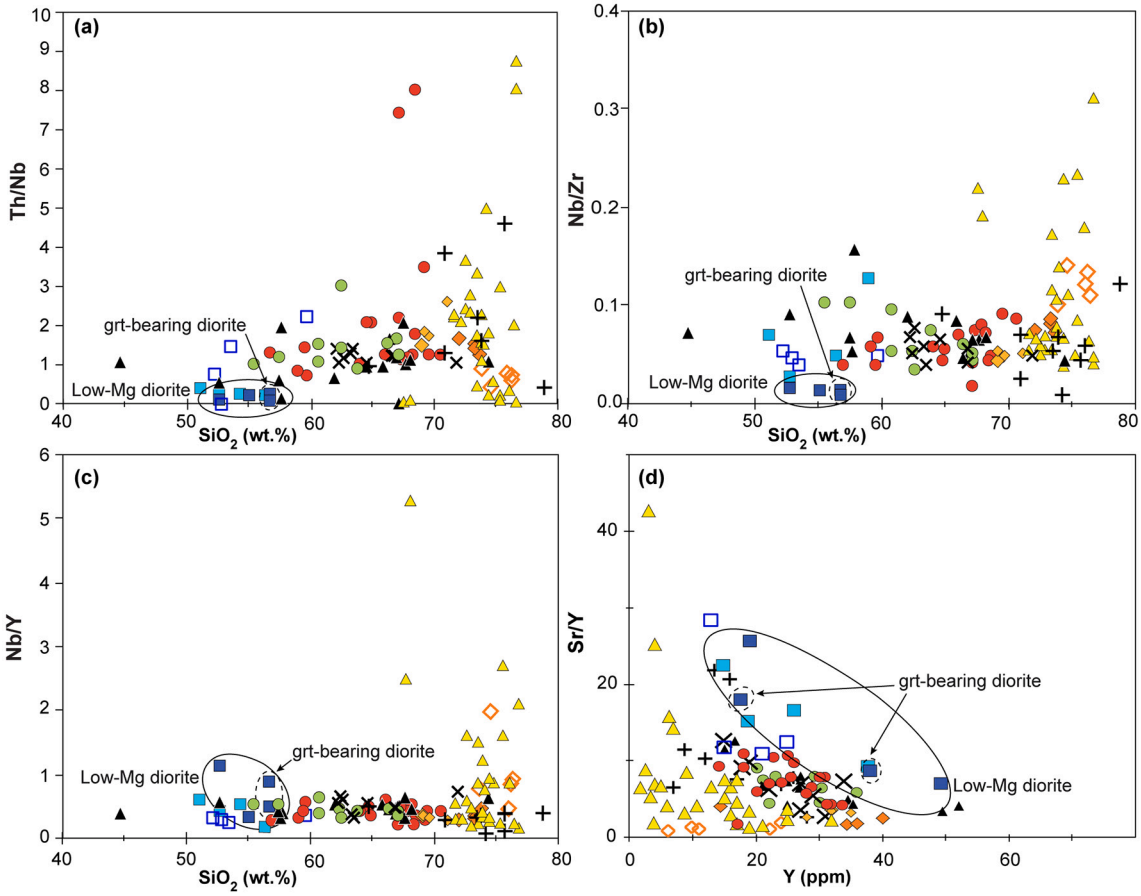

Fig. 9. Geochemical diagrams showing essential variations of selected trace elements (a) Th/Nb; (b) Nb/Zr; (c) Nb/Y versus SiO_2 (wt%); and (d) Sr/Y versus Y from the Ceret and Mas Claret mafic complexes, SL–LJ pluton, leucogranites, orthogneisses, metapelites and migmatites. Symbol legend in Fig. 5.

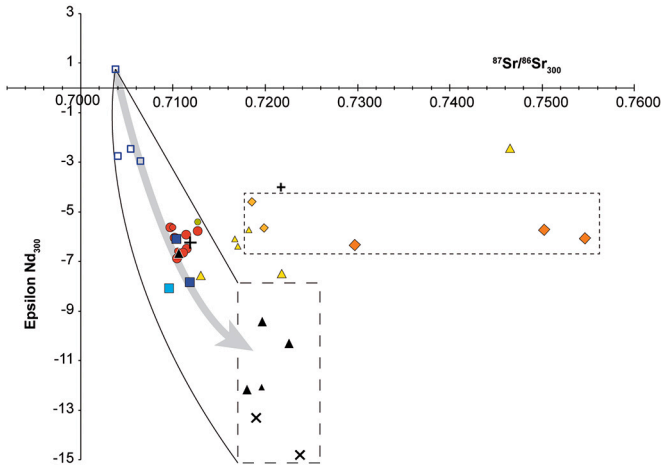

Fig. 10. ($_{143}Nd/_{144}Nd$) versus. ($_{87}Sr/_{86}Sr$) diagram at 300 Ma showing the Sr—Nd isotopic compositions of the magmatic rocks from the Ceret and Mas Claret mafic complexes, SL–LJ pluton, leucogranites, and orthogneisses, metapelites and migmatites from the Roc de Frausa and L'Albera massifs. Curves represent mixing hyperbolas between different metamorphic rocks and an ultramafic cumulate. The vertical rectangle represents hypothetical compositions of melts derived from metamorphic rocks that mixed with the ultramafic cumulate to give compositions similar to those of mafic complexes (plotted in light and dark blue squares) and the SL–LJ pluton (red circles). Symbol legend in Fig. 5. (For interpretation of the references to colour in this figure legend, the reader is referred to the web version of this article.)

range of middle to upper continental crust.

6. P–T conditions of crystallization and emplacement depth of the Ceret mafic complex

6.1. Mineral chemistry of mafic rocks

Analyses of amphibole, biotite and plagioclase were carried out for garnet-bearing and garnet-absent diorites from the Ceret mafic complex and for gabbros from the Mas Claret mafic complex (Fig. 11a-d). Moreover, garnet profiles were performed on three representative garnet-bearing diorites (Fig. 12). Electron microprobe analyses of amphibole, garnet, biotite, and plagioclase of representative samples are calculated in cations per formula unit (p.f.u.) and are summarized in Tables S7 to S11. Details of the methodology can be found in Appendix A.2 of the Supplementary Material.

6.1.1. Amphibole

Amphibole is classified according to the IMA recommendations (Hawthorne et al., 2012). Fe—Mg amphibole belongs to the cummingtonite – grunerite series; and in diorite it is grunerite rich (Fig. 11a). It has a very low MnO content (0.43–1.14 wt%) and a positive correlation of Mn with Fe (Fig. 11a, Table S9). The X_{Mg} ratio is variable depending on the sample (0.39–0.16) but amphibole from garnet-bearing diorite is richer in Mg than that of the garnet-free diorite sample. TiO_2 varies between 0 and 0.47 wt%. Al^{IV} values are between 0.09 and 0.75 p.f.u. Based on the IMA recommendations, calcic amphibole is classified as hornblende or tschermakite (Fig. 11b, Table S10). It has an X_{Mg} from 0.26–0.1, TiO_2 from 0 to 1.59 wt%, CaO from 8.86–11.31 wt% (being

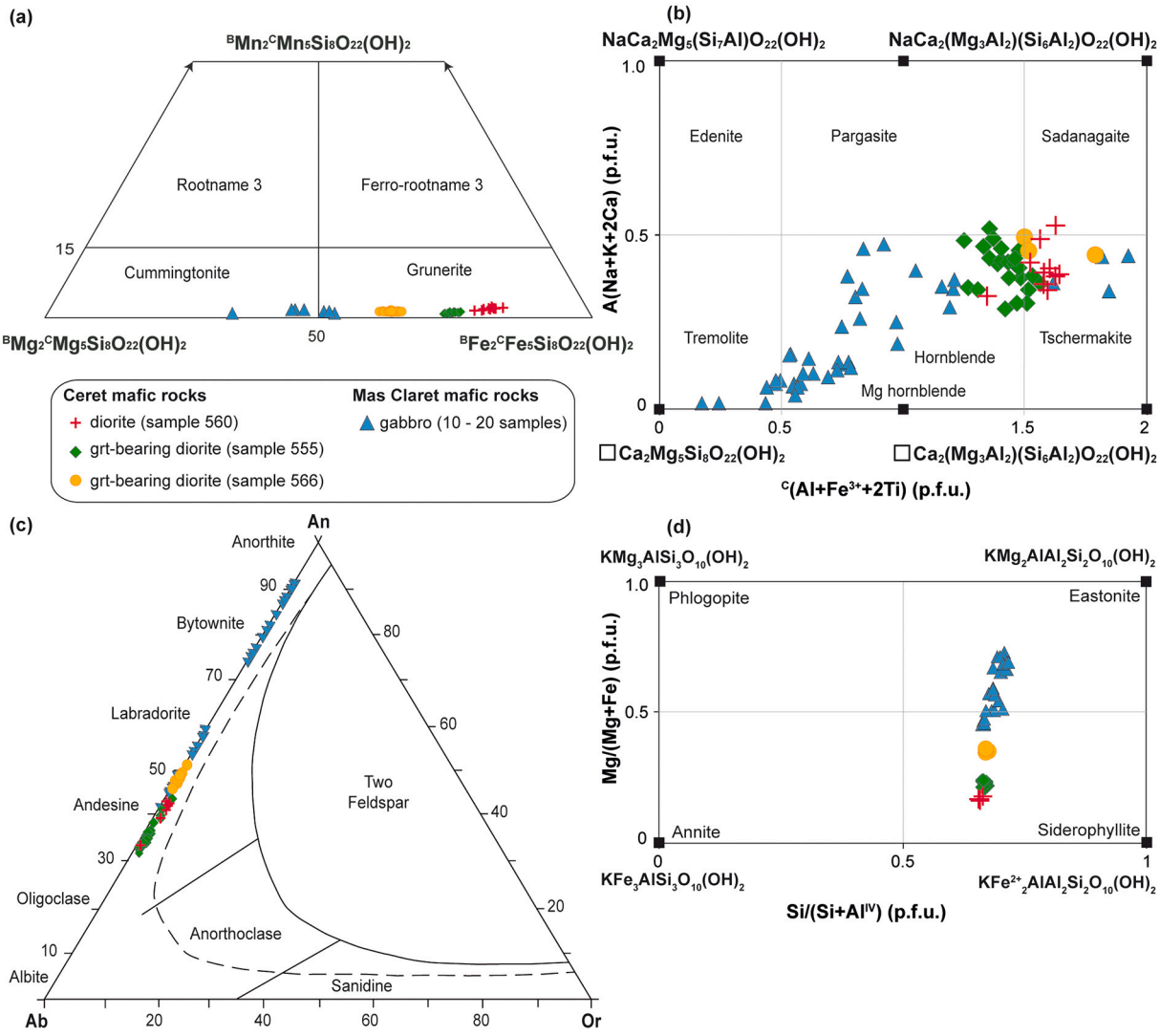

Fig. 11. Compositional ranges of (a) Fe—Mg amphibole, (b) Ca amphibole, (c) plagioclase and (d) biotite. Abbreviations used for feldspar end-members in molar proportions are: An = Ca / (Ca + Na + K), Ab = Na / (Ca + Na + K) and Or = K / (Ca + Na + K).

poorer in Ca for garnet-bearing diorite) and MnO from 0.15–0.51 wt%. The Al^{IV} value has a remarkable variation (1.51–2.17 p.f.u.), although its content is much higher than that of grunerite. In gabbro, the cummingtonite – grunerite amphibole is richer in Mg than that of diorite (X_{Mg} = 0.47–0.66; Fig. 11a). Ca amphibole is classified as hornblende (Mg-hb, Mg-ferri hb, Fe-ferri hb), Fe-tschermakite or tremolite (Fig. 11b).

6.1.2. Plagioclase

Plagioclase in diorite is poorly zoned. Anorthite content ranges from An51 (core) to An32 (rim), being lower in garnet-bearing diorite (Fig. 11c, Table S7). It is locally altered to sericite. In gabbro, plagioclase is zoned and its An content ranges from An92 (core) to An43 (rim) (Fig. 11c).

6.1.3. Biotite

In diorite, biotite has a fairly constant composition (Fig. 11d, Table S8). It can be classified as siderophyllite with an X_{Mg} (Mg/(Fe^{2+}+Mg)) ratio ranging from 0.16–0.36 in garnet-absent diorite and 0.76–0.84 in the garnet-bearing diorite. TiO_2 content (2.38–4.11 wt%) and Al^{IV} (1.29–1.38 p.f.u.) are also higher in garnet-bearing diorite. In gabbro, biotite ranges from siderophyllite to eastonite. It is more Mg-rich than that of diorite and its X_{Mg} ratio ranges from 0.45 to 0.72 associated with an increase in the Si/(Si + Al^{IV}) ratio from 0.66–0.71 (Fig. 11d).

6.1.4. Garnet

Garnet has a fairly constant compositional profile in the cores of all samples and variable zoning towards the rims, depending on the sample (Fig. 12, Table S11). In spite of the fact that the composition is not constant across all garnets, the core generally has higher pyrope and almandine contents, which decreases towards the intermediate core-rim points, followed by a slight increase in almandine at the rim. Grossular content displays an opposite trend to that of almandine. $X_{Fe(tot)}$ (0.90–0.96) is high and it shows an increasing trend towards the rims, with an opposite trend to that of pyrope.

6.2. Forward modeling

A *P–T* pseudosection was calculated for a garnet-bearing diorite (sample 566) since garnet and amphibole are pressure sensitive (Fig. 13a–e). We used Theriak-Domino software (version 15.r187-gf; Capitani and Petrakakis, 2010) with the ds62 dataset (Holland and Powell, 2011; February 2012 upgrade) in the chemical system

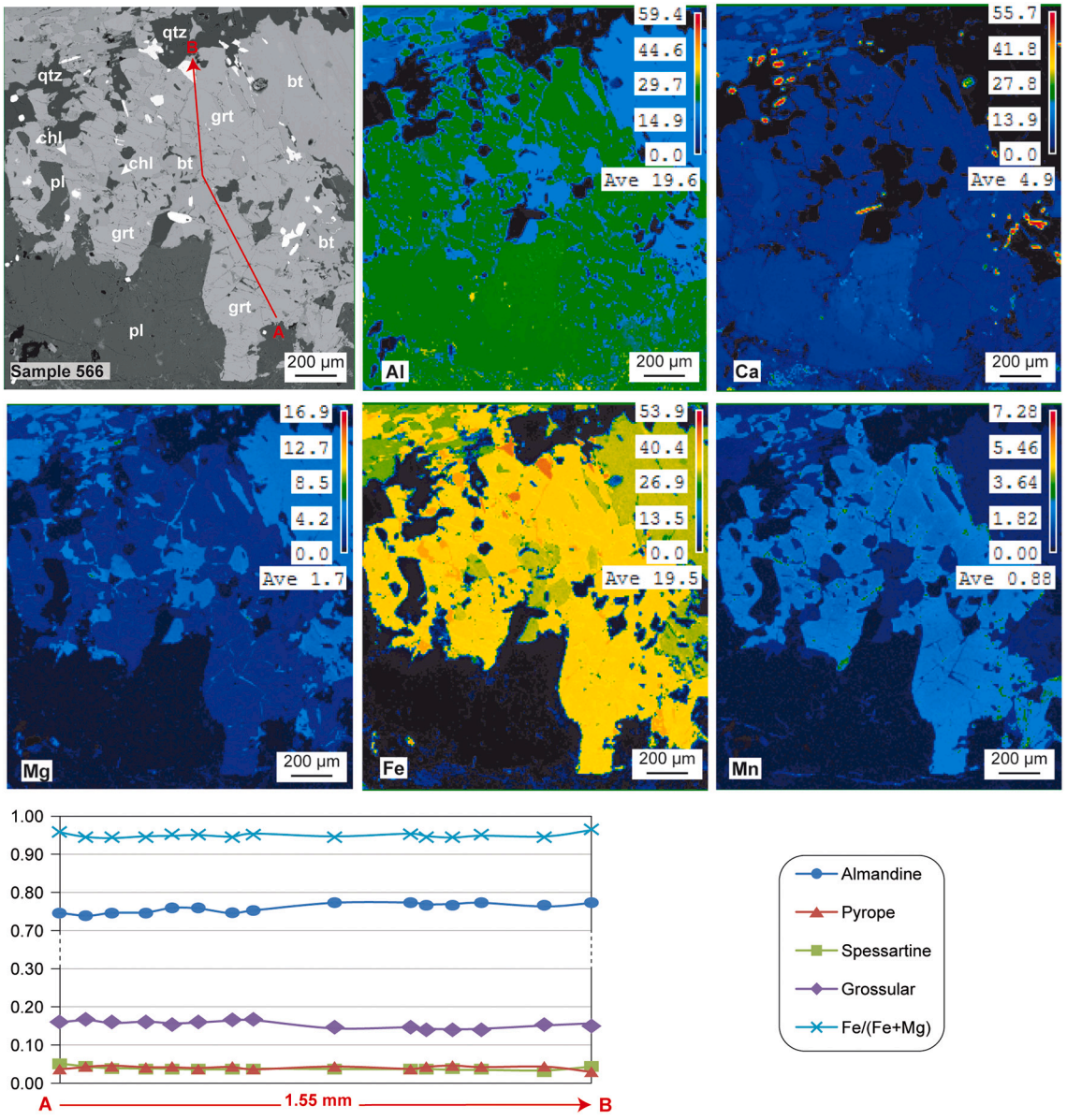

Fig. 12. Chemical zoning maps and garnet profile from a representative garnet-bearing diorite (Sample 566). End-members in molar proportions: almandine (alm) = Fe / (Ca + Fe + Mg + Mn), pyrope (prp) = Mg / (Ca + Fe + Mg + Mn), spessartine (sps) = Mn / (Ca + Fe + Mg + Mn), grossular (grs) = Ca / (Ca + Fe + Mg + Mn) and X_{Fe} = Fe / (Fe + Mg).

Na_2O–CaO–K_2O–FeO–MgO–Al_2O_3–SiO_2–H_2O–TiO_2–O (NCKFMASHTO). Details of the methodology can be found in Appendix A.3 of the Supplementary Material.

In the *P*–*T* pseudosection, constructed for 1.1 wt% H_2O, an Fe—Mg amphibole (grunerite) is stable at 700–760 °C and 0.4–0.8 GPa (green isopleths in Fig. 13b). Two separate stability fields exist for Ca-amphibole (Fig. 13b): a narrow one with Ca-amphibole (pargasite) that is stable above 760 °C for a wide range of pressure (around 0.4–0.8 GPa) and a lower *P*–*T* field with Ca-amphibole between 650 and 730 °C and 0.4–0.625 GPa (orange isopleths in Fig. 13b). The presence of gruneritic amphibole and garnet (see Fig. 4a–b) is compatible with the stability field containing qz-pl-grt-bt-camp-ilm-liq at around 0.55–0.8 GPa and 650–750 °C (Fig. 13a). The analyzed X_{Mg} value of the Fe—Mg amphibole in the sample (X_{Mg} = 0.18) fits with the calculated isopleths of grunerite in the qz-pl-grt-bt-camp-ilm-liq field at around 0.6 GPa and 750 °C (Fig. 13b). The corona of Ca-amphibole around Fe—Mg amphibole observed in the sample (Fig. 4a) is consistent with a path that evolved from a field containing grunerite + garnet (qz-pl-grt-bt-camp-ilm-liq) into a field defined by a Ca-amphibole but without garnet (qz-pl-bt-camp-ilm-liq; Fig. 13b). The X_{Mg} of the Ca-amphibole analyzed in the sample (X_{Mg} = 0.10; Fig. 11b) is similar to that predicted by the pseudosection at the solidus at around 0.55 GPa and 680 °C where the rock completely crystallized. However, we must point out that the model predicts pargasite for the Ca-amphibole, whereas the analyzed Ca-amphibole is a hornblende – tschermakite (see Fig. 11d). In spite of this, we have assumed that the discrepancies in Ca-amphibole can be mostly related to the solution models used, as explained in Appendix A.3. In addition, corresponding garnet isopleths (X_{Fe} = 0.93, X_{alm} = 0.72–0.74 and X_{grs} = 0.18–0.21; Fig. 13c) match the analyzed composition of garnet for Sample 566 (X_{Fe} = 0.94; alm = 0.77; grs = 0.15; Fig. 12) in the qz-pl-grt-bt-camp-ilm-liq field at around 0.6 GPa and 750 °C. The nearly isobaric path from the qz-pl-grt-bt-camp-ilm-liq field at 750 °C and 0.6 GPa to the final phase assemblage field of qz-pl-bt-camp-ilm at 0.55 GPa and 680 °C crosses the garnet-out line at around 720 °C. Therefore, garnet in this sample is metastable with respect to the final phase assemblage field of qz-pl-bt-camp-ilm at the solidus, as is also

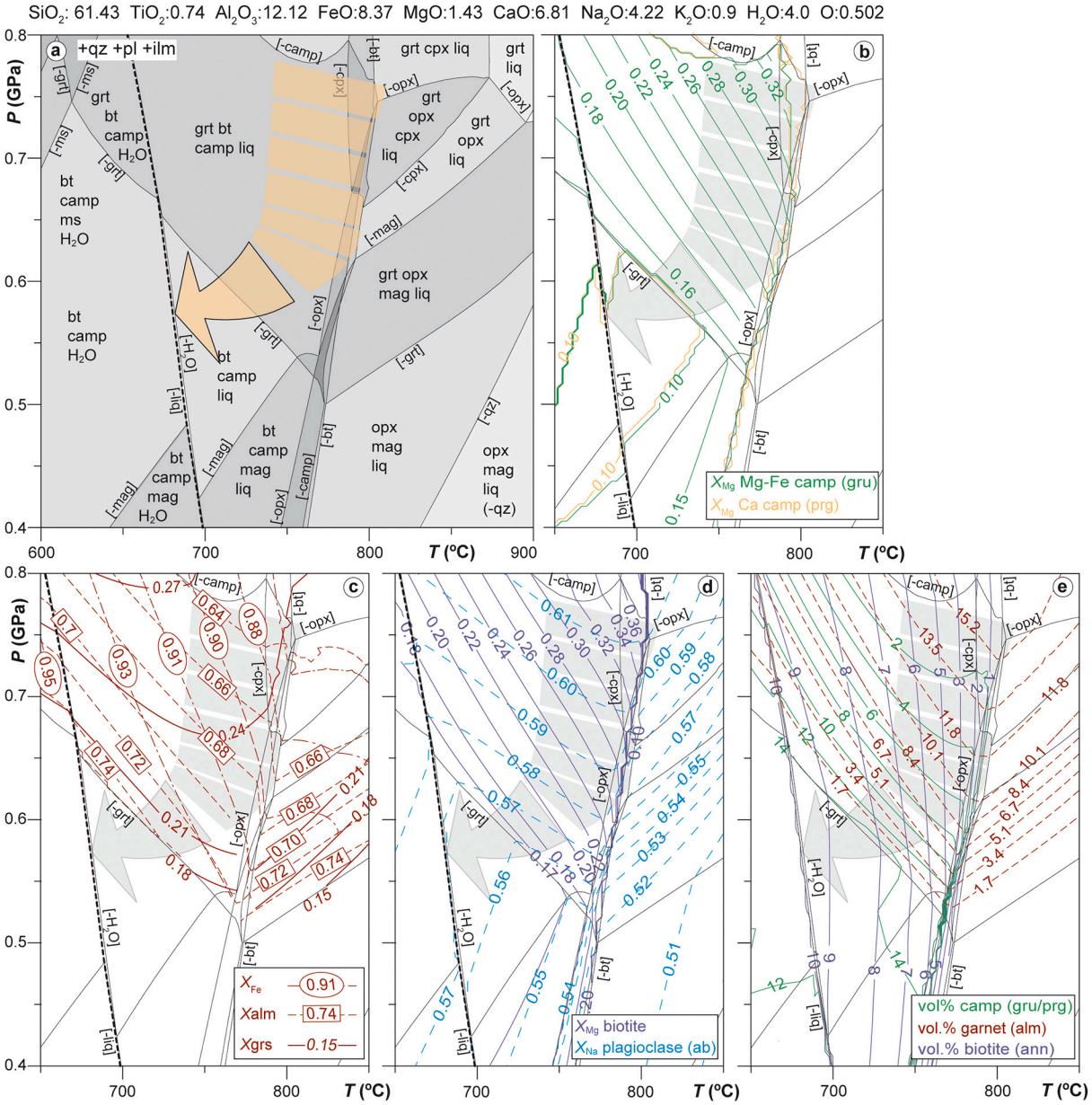

Fig. 13. (a) Closed-system *P–T* pseudosections calculated for a representative garnet-bearing diorite (sample 566) from the Ceret mafic complex. (b – e) Simplified pseudosections with compositional isopleths for the X_{Mg} ratio of Mg—Fe clinoamphibole (grunerite) and Ca clinoamphibole (pargasite); X_{Fe} ratio, almandine (X_{alm}) and grossular (X_{grs}) in garnet; X_{Mg} ratio of biotite; albite content of plagioclase (X_{Na}); and molar proportions of clinoamphibole, garnet, and biotite (in vol%). The solidus is underlined by a thick black dashed line. See text for discussion of the *P–T* path. Mineral abbreviations in Fig. 3.

indicated by the coronas of biotite, plagioclase, and quartz around garnet (Figs. 2f, 4b). The coronas suggest a late peritectic reaction between garnet and the metaluminous quartz diorite melt to consume the garnet. Biotite and plagioclase were equilibrated at the solidus (680 °C and 0.55 GPa) with X_{Mg} and X_{Na} isopleths similar to the analyzed biotite (X_{Mg} = 0.16–0.17) and plagioclase (ab = 0.57) (Fig. 13d).

The mineral modes calculated from the petrography were also compared with the isopleths of modal abundance (in vol%) for amphibole, garnet, biotite and plagioclase on the calculated phase diagram (Fig. 13e). Near the solidus, at 680 °C and 0.55 GPa, the model predicts around 13 vol% amphibole, 60 vol% plagioclase, 16 vol% quartz, and 11 vol% biotite. These modes provide quite a good match to the percentages of amphibole (18%), plagioclase (53%), and quartz (10%) calculated for Sample 566, but not for biotite (20%). Moreover, the retrograde isobaric path shows an increase in amphibole (from 9 to 13 vol%) and biotite (from 7 to 10 vol%), which is in accordance with the overgrowing coronas of Ca-amphibole around Mg—Fe amphibole and biotite around garnet (Fig. 4a, b).

The path followed by the garnet-bearing diorite is consistent with the observed textures, compositions of the phases and modes (Fig. 13a–e), and it can be considered representative of the latest stages of magmatic crystallization of diorite and gabbro from the mafic complexes. This path registered decompression from 0.8–0.75 GPa at P–T peak conditions to 0.55 GPa followed by a retrograde path. Garnet crystallized at a higher pressure and was consumed on its way up the crust along with decreasing temperature and pressure (see dashed path in Fig. 13). These *P–T* conditions indicate that the paleodepth of emplacement at which the gabbro finished its crystallization was around 20 km (considering a mean density of the rock column of 2800 kg/m^3). According to the maximum pressure registered (0.8–0.75 GPa), the path of the gabbro can be traced back to around 27 km depth.

7. Discussion

The compiled data allow us to discuss on the various aspects covered in this paper such as the emplacement mechanisms of the SL-LJ plutonic suite, the magmatic evolution of the suite and the water content of the magma. We argue on the mantelic or crustal origin of magmas and we conclude with the magmatic history of the several intrusive bodies in the regional tectonic regime.

7.1. Emplacement mechanisms and prevailing regional tectonic regime

The interference pattern resulting from the superposition of Variscan (F2) and Alpine (F3) folding in the Eastern Pyrenees gives an exceptional field example to infer the 3D geometry of the SL–LJ pluton and its associated igneous rocks. The southern flank of the antiform involving the entire Roc de Frausa Massif and the SL–LJ pluton cuts through a complete section of the pluton (Fig. 1). In this flank, the relation between thickness (~ 3.5 km) and longitude (~ 40 km) displayed by the SL–LJ pluton can be calculated from the map pattern and cross-section and falls within the field of plutons and batholiths according to the empirical law of Cruden and McCaffrey (2001). The intrusion feeder zones are located in the northern flank of the antiform where the mafic complexes crop out, cutting the deeper structural levels of the Roc de Frausa and L'Albera series (Fig. 1b,c).

The floor of the pluton is located above the Upper Proterozoic – Mid-Ordovician sequence, which is largely parallel to the S1 foliation, and the roof is slightly oblique to the Upper Ordovician-Silurian sequence (S0) (Fig. 1b). This parallelism together with a well developed magmatic

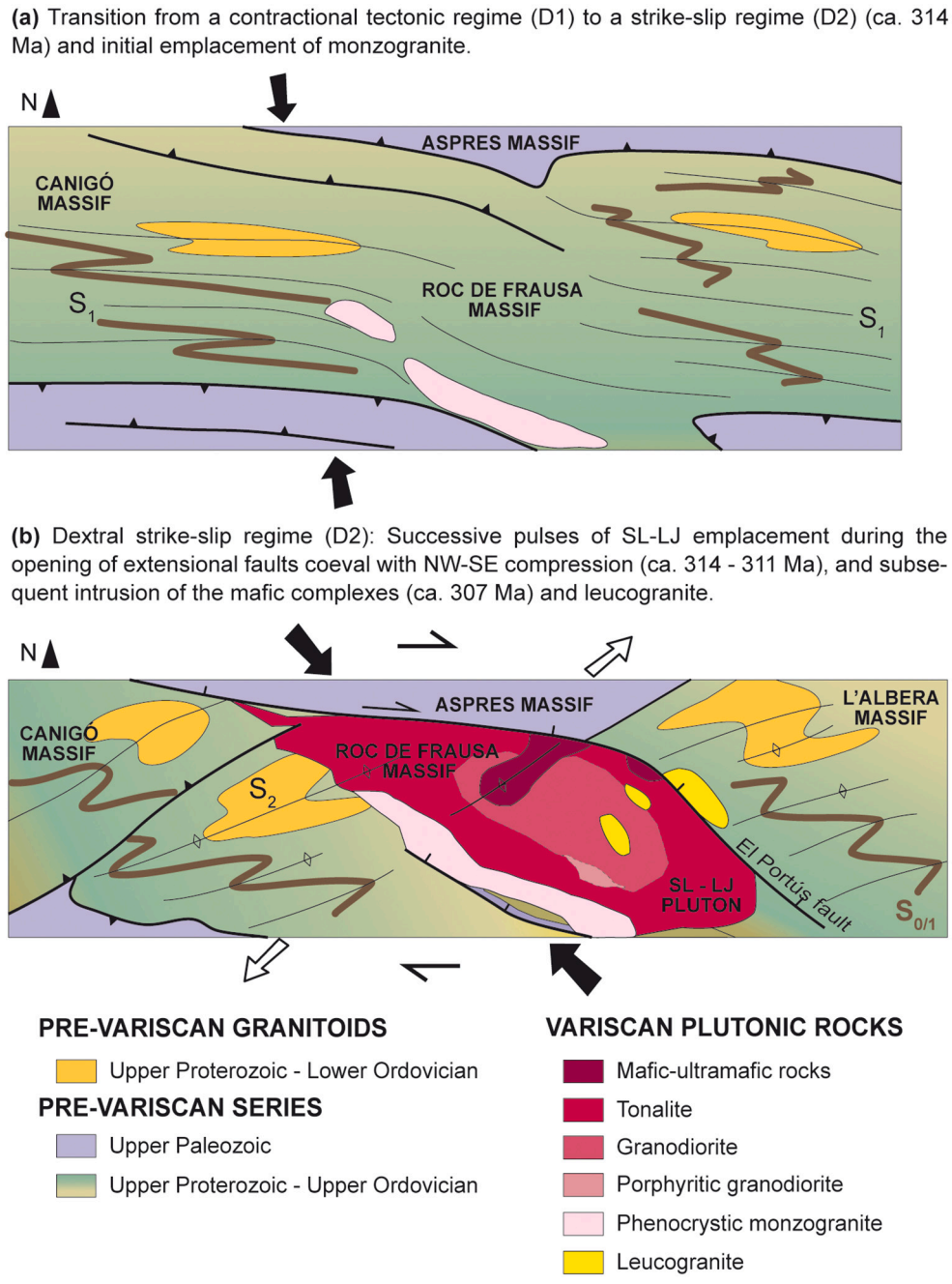

Fig. 14. Depth slices (a and b) showing a model for the emplacement of the SL–LJ pluton, mafic complexes and leucogranites in a dextral strike-slip context. The SL–LJ pluton intruded in dextral strike-slip faults, coeval with NW-SE contractional features of D2.

and magnetic fabric parallel to S1 suggests that initial phases of intrusion of SL–LJ magmas took place at the end of D1, at ca. 314–311 Ma (Aguilar et al., 2014; Olivier et al., 2016). At the emplacement level, the intrusion spread concordant to the main discontinuities. The floor level was located at a deep structural level in the sillimanite – migmatite zones and the roof was located at the biotite zone in the Upper Ordovician and the Silurian black shales, the most important detachment level in the Variscan system. The lack of stratigraphic continuity above and below the pluton suggests that the stratigraphic succession of the L'Albera massif was laterally displaced, and the intruding magma progressively grew while cutting through the entire sequence and filling the available space. This placement of the magmas is compatible with a local extensional setting that favoured the ascent of the SL–LJ magmas from a lower crustal reservoir (discussed in Section 7.4) through vertical feeder zones in the footwall of the extensional faults where lithostatic pressure was minimal (Fig. 14a). The feeder zones, as well as the deep structural levels underneath the Triassic unconformity are located in the footwall of the Banys d'Arles thrust, whereas a thick Cambrian – Upper Paleozoic low-grade metamorphic succession (Aspres massif) is preserved in the hangingwall (Fig. 1c). Thus, a restoration of this thrust shows a late Variscan extensional fault that was reactivated during the Pyrenean deformation.

The coeval development of NW-SE to NNW-ESE extensional faults with the NE-SW trending D2 contractional structures and the horizontal attitude of the mineral lineations, once restored the Alpine deformation, is compatible with a regional dextral strike-slip tectonic setting that took place during and after the emplacement of the igneous bodies. Upward melt migration was also enhanced by D2 contractional structures as suggested by other authors (Vigneresse and Tikoff, 1999) for other locations. The mafic complexes were emplaced in the feeder zones at a later stage during the development of NE-SW trending D2 contractional structures (Fig. 14b), as shown by the preferred orientation of S2 magmatic fabric and the absolute dating (ca. 312–307 Ma; Aguilar et al., 2014, 2015).

The Ceret mafic complex registers a decompressive path from 26 to 27 km (~ 0.75 GPa) at 750 °C to a final emplacement depth of 19–20 km (~0.55 GPa) at solidus during D2 (considering a mean density of the rock column of 2800 kg/m^3) (Fig. 13). Decompressive paths are also recorded by the country-rocks located at the Ceret contact aureole from ~0.85 GPa to ~0.55 GPa followed by a retrograde path at a *P* of around 0.55 GPa and by metamorphic rocks located at different structural levels (Aguilar et al., 2015, 2016; Vilà et al., 2007). All these paths are indicative of a progressive exhumation of deep structural levels and would be compatible with local extensional structures coeval with diapiric uplift or dome development. These two exhumation mechanisms can be coeval and are consistent with the proposed dextral strike-slip tectonic setting. The paths also constrain the paleodepth of the floor of the overlying SL–LJ pluton that was located at around 12–15 km (~ 0.3–0.4 GPa).

Further west in the Pyrenees, other Variscan plutons such as the Andorra-Mont-Lluís and La Maladeta (Arranz, 1997; Roberts et al., 2000; Soler and Enrique, 1989) were emplaced at a similar depth as the SL–LJ pluton. Structurally above them, NW-SE extensional basins were formed, oblique to the Alpine E-W structural trend. These basins are interpreted as pull-apart extensional basins related to a regional dextral strike-slip setting (Gisbert, 1984; Lloret et al., 2018; López-Gómez et al., 2002) and host calc-alkaline volcanic rocks (ignimbrites to andesites) that are coeval with the emplacement of the plutons at depth, with ages ranging from ca. 304 Ma to 266 Ma (Upper Carboniferous – Mid-Permian) (Pereira et al., 2014). The SL–LJ pluton likely belongs to the early stages of the same intrusive system and related volcano-sedimentary Late Variscan basins. In the Eastern Pyrenees the upper structural levels and the Carboniferous – Permian extensional basins are preserved westward of the study area in the Cadí thrust sheet that has been interpreted to root in the Banys d'Arles thrust (Muñoz et al., 1986).

7.2. Constraints on the evolution of magmas

Chemical variation of significant trace and major elements trends and ratios of the entire igneous SL–LJ suite indicates that the most important processes that acted on the differentiation of magmas were the contamination/assimilation of crustal rocks and crystal fractionation. In this section, the processes involved in the three groups of rocks will be discussed separately.

7.2.1. SL–LJ granitoids

Contribution of crustal components to SL–LJ granitoids is recorded by the Sr and Nd isotopic ratios that depart from the mantle array (Fig. 10a). This is supported by LILE enrichment relative to HFSE (Fig. 8f), which is dominant in granitoid suites regardless of their inferred origin (e.g., crustal partial melting —Caledonian type—, or through differentiation of mantle-derived melts which originate from a variable subduction-modified mantle wedge —Cordilleran type—). The crustal component was not acquired at shallow levels, but instead originated at deeper crustal levels or in the mantle. This is suggested by the chilled margins of the main granodiorite – tonalite intrusion of SL–LJ pluton that indicate a strong contrast in temperature between the magma and the host rocks, and absence of significant interaction (i.e., assimilation) at the final emplacement location of the magma. Nearly homogeneous Sr and Nd isotope ratios, not correlated with differentiation indexes (e.g., SiO_2), suggest that the entire SL–LJ suite, including the early-intruded monzogranites, were originated from a single magma batch, which was homogenized prior to final magmatic differentiation, pointing to a hybrid source instead of crustal contamination. Trace element ratios and sub-parallel patterns in multi-elemental trace element diagrams (Figs. 8–10) also preclude crustal assimilation after homogenization. Homogenization of the magma occurred in a deep reservoir prior to differentiation, ascent and final emplacement, as imposed by the separate early emplacement of monzogranites relative to the rest of the SL–LJ pluton (see Section 7.5).

Final magma differentiation (after homogenization) was predominantly controlled by fractional crystallization. Decreasing Al_2O_3, TiO_2, FeO, MgO and CaO, nearly constant Na_2O, and increasing K_2O as a function of SiO_2 (Fig. 5b-h) are consistent with a fractionating assemblage that includes amphibole, plagioclase, and biotite. Indeed, major element compositions of SL–LJ rocks follow a calc-alkaline differentiation trend (Fig. 6), which is also shown by the cotectic line suggested by Castro (2013, 2020, 2021) (Fig. 7). The curved trend defined by the fractionation of MgO versus SiO_2 approximates the cotectic relations displayed by experimental liquids and is common to Iberian and Caledonian I-type granites, as well as to Cordilleran plutons (Castro, 2013; Figs. 6, 7). Evidence for dominant fractional crystallization processes can also be found in the high concentration of light REE and by the nearly parallel trends of REE patterns in the average chondrite-normalized diagram (Fig. 8a, b, c). The increasing negative Eu anomaly as a function of the degree of differentiation (Fig. 8a, b) is consistent with plagioclase and amphibole fractionation, which is mostly evident in the tonalites at the base of the magma chamber. Also compatible with the fractionating assemblage are the increasing negative anomalies in Ba, Ti, Sr, and P (Fig. 8f), which include apatite, the strong negative correlation of Zr with SiO_2 (Fig. 5a)—indicating zircon fractionation—and the slightly positive correlation of Th/Nb against SiO_2 (Fig. 9a). The higher concentration of REE also indicates a higher percentage of fractionation of SL–LJ granitoids compared to the magmas which form the mafic complexes.

7.2.2. Mafic complexes

Mas Claret mafic rocks represent the most primitive magmas in the study area. Their Sr and Nd isotope ratios indicate a dominant mantle source with only a minor crustal contribution (Fig. 10, Table S6). For major elements, the low TiO_2 and FeO alongside the high MgO content of the Mas Claret magma (Fig. 5c-e) can also be explained by a dominant

mantle origin with a low crustal contribution. For Ceret mafic rocks, the more radiogenic Sr and less radiogenic Nd isotope ratios compared to Mas Claret suggest a larger crustal contribution and/or participation of a more isotopically evolved crustal reservoir during their genesis or evolution, similarly to the SL–LJ rocks (Fig. 10).

Trace element patterns of mafic rocks (Fig. 8), although broadly parallel, are less regular than those of the SL–LJ rocks, suggesting a more complex origin. The positive Eu anomaly for most Ceret samples and the slightly positive Eu anomaly for one Mas Claret sample may indicate either a cumulate component or assimilation of feldspar- and/or amphibole-bearing rocks. This is consistent with petrographic observations, which point to a cumulitic character for some of the most mafic rocks. In contrast to SL–LJ, the presence of abundant cumulates in mafic complexes shows significant magma differentiation by fractional crystallization at the final emplacement depth. In regular-Zr Ceret mafic rocks, major element compositions close to the differentiation trend of SL–LJ granitoids are compatible with a fractionating assemblage that includes amphibole and plagioclase. In the mantle-normalized diagram (Fig. 8), trends of mafic rocks depart from common calc-alkaline ones like those depicted by the SL–LJ rocks. Instead, local anomalous element enrichment (e.g., Ba, P, and more remarkably Zr in high-Zr rocks) further support a cumulate component and/or assimilation of cumulate or restitic rocks that were coeval with crystal fractionation. In other areas, the presence of a positive Ba anomaly has been related to contamination by previously depleted crustal material (e.g., Voshage et al., 1990). The increase of Th/Nb with SiO_2 for Mas Claret rocks is consistent with differentiation being mostly controlled by fractional crystallization with no significant assimilation, whereas the nearly constant low Th/Nb ratios for Ceret rocks (Fig. 9a) suggest assimilation of cumulate/restitic rocks (of a low Th/Nb component) that were coeval with crystal fractionation.

A larger effect of crustal assimilation can be interpreted from the high CaO/MgO ratios in gabbro, diorite and tonalite from the Ceret mafic complex (Fig. 7a). In high-Zr rocks, crustal assimilation is also registered for higher FeOt and Na_2O, and for lower MgO differentiation trends (Figs. 5b, 7b) that shifted from the experimental cotectic line of Castro (2013) (Fig. 7a). In garnet-bearing diorites evidence for crustal assimilation is provided by the presence of garnet, a Mg-richer grunerite, and a Ca-poorer hornblende, compared to garnet-absent diorites (Fig. 11a-d, Tables S7–10). From the data we consider that high-Zr rocks assimilated an additional component compared to regular-Zr magmas, which was responsible for the changes in major element chemistry and Zr enrichment. The Zr-rich component was assimilated during the final stages of magma differentiation as deduced from the heterogeneity of some major and trace element content (Figs. 5b, 8e). In the Sesia area (Alps), high Zr content of garnet-bearing igneous rocks was attributed to assimilation of biotite-rich restitic material from which a partial melt was previously extracted (Sinigoi et al., 2011). However, in the high-Zr Ceret rocks, the composition of the assimilated rock does not correspond to that of host metapelites and migmatites. Remarkably, high-Zr rocks show no increase in K_2O and their CaO content is much higher than that of metapelites; trace elements reveal another contaminant (Fig. 7a, c, d). Since the local host rock is not a suitable contaminant, this component was likely acquired during magma stagnation in the lower crust. Given the isotopic similarity between the SL–LJ and Ceret magmas, cumulitic or restitic material from the same reservoir may have been assimilated, although the more evolved isotopic compositions require another component. Vilà et al. (2005) suggest that the magma that formed the SL–LJ pluton was generated by partial melting of metatonalites in the lower crust. The metatonalites could also be the contaminant of Ceret magmas. Nevertheless, the scarce number of analyses precludes further discussion on the composition of the contaminant.

7.2.3. Origin of garnet in mafic rocks

Garnet can crystallize from intermediate calc-alkaline melts at pressures exceeding 0.8 GPa. Several mechanisms were proposed to explain the presence of garnet in metaluminous mafic rocks. They include considering garnet as a restitic, xenocrystic, anatectic, or primary magmatic phase, among other origins (Clarke and Rottura, 1994).

In the studied area, textural relations, trace element geochemistry, pseudosection modeling and mineral chemistry favour garnet growth as a cumulus phase from a contaminated magma at depth. Textural relations suggest that garnet in high-Zr Ceret rocks is an early magmatic phase, together with grunerite and plagioclase, as the three minerals are in mutual contact. In addition, garnet is not in contact with hornblende, which is a late mineral. A corona of plagioclase, biotite and quartz suggests a late peritectic reaction with the metaluminous magma in order to consume garnet (Figs. 2f, 4b).

Mas Claret and some Ceret rocks show no HREE enrichment or depletion, suggesting no significant control of garnet during the genesis or evolution of these magmas. On the contrary, the flat to slightly concave upward pattern of the HREE of several diorite samples and the positive slope for HREE of one of the garnet-bearing diorites point to a less fractionated pattern of mafic rocks with respect to the rest of the analyzed rocks as well as the involvement of garnet as a cumulus phase. The high Sr/Y ratio and low Y (Fig. 9d) in some mafic rocks can be interpreted as resulting from the initial magma forming at high pressure in equilibrium with garnet, which retained Y (Moyen, 2009). In contrast, mafic rocks with low Sr/Y and high Y can represent cumulates in equilibrium with garnet as suggested by one of the garnet-bearing diorites (Sample 555) (Fig. 9d).

Pseudosection modeling shows that garnet grew peritectically at a pressure above 0.6 GPa and 750 °C for a garnet-bearing diorite (Sample 566; Fig. 13a–e). The pressure stability field of garnet widens to lower pressures with higher magma Fe content, whereby high-Zr Ceret magmas were enriched compared to the rest of the magmatic suite. The flat composition of garnet from Sample 566, for example, (alm = 0.74–0.77; pyp = 0.04–0.05; sps = 0.04–0.05; grs = 0.01–0.02; X_{Fe} = 0.94–0.96; Fig. 12), together with its inclusion-free core, are consistent with continuous growth from a homogeneous melt. In contrast, garnet from metapelitic xenoliths included in the diorite/gabbro and from the inner contact aureole has inclusions of sillimanite and biotite. Its composition is different than that of the garnet in the mafic complexes and it has a more complex profile (alm = 0.68–0.78; pyp = 0.12–0.28; sps = 0.02–0.04; grs = 0.04–0.08; X_{Fe} = 0.72–0.91, Aguilar et al., 2016). This precludes an origin of garnet from contamination by metapelites.

Thus, garnet likely formed as an early magmatic phase at depth and was metastably preserved in the Fe-rich garnet-bearing diorite and gabbro by fast cooling and system quenching during its final emplacement at lower pressures. This further supports the notion that the main magma evolution took place at depth and that the ascent and emplacement at its final location was comparatively fast.

7.2.4. Leucogranites

The isotopic and chemical composition of leucogranites strongly differ from those of the SL–LJ pluton and mafic complexes. Whereas Nd isotope compositions are similar to those of the other magmas, Sr isotope ratios range from comparable compositions to much more radiogenic ones. Trace element concentrations in leucogranites are lower than in the other magmatic suites and they are significantly depleted in REE. These compositions largely preclude a genetic relationship of leucogranites with SL–LJ granitoids or mafic magmas by extreme fractional crystallization processes. Instead, they point to an origin from partial melting of a crustal source with restitic phases holding REE. The presence of migmatites at the deeper outcropping levels and at the contact with the mafic rocks provide evidence for the occurrence of anatectic melting in the area. Leucosomes from metapelites show depletion in many trace elements, particularly in REE compared to melanosomes or non-migmatitic rocks. Major and trace element and isotope compositions of leucogranite, in addition to its peraluminic character, are consistent with partial melting of both high- and low- $^{143}Nd/^{144}Nd$ populations from local metapelites and orthogneisses (Fig. 7). Absence

of HREE depletion in leucogranite indicates that garnet was not a restitic phase, thus it was likely not present in the source rock. The nebulitic texture of some leucosomes in high grade domains and the blurred contacts between leucogranite and metamorphic country rocks suggest that leucosome lenses coalesced to form larger leucogranite bodies, and a similar mechanism may have occurred with partial melts from orthogneisses. Locally, blurred contacts between leucogranites and SL–LJ granitoids may also indicate that leucogranites were emplaced prior to complete solidification or cool down of granites, thus some interaction may have occurred. Partial melting of orthogneiss as a source for leucogranite was already suggested by Vilà et al. (2005), although, as seen, a metapelitic component is also required. Participation of deeper rocks of similar compositions to the ones cropping out in the studied area should also be considered as a possible source of leucogranite.

Indeed, individual leucogranite bodies likely represent mixtures in variable proportions of metapelites (+/− orthogneisses), which can explain their full compositional range. To illustrate this, a multielement mass balance was calculated by mixing two end-member compositions: a mean leucogranite (L) calculated from 29 analyzed samples and a residual melanosome (R), corresponding to the most restitic migmatite from the area (Sample 462; Aguilar et al., 2016). The composition of the metapelite representing the protolith (P) is an average of 13 analyzed non-migmatitic metapelites. The equation used is:

$$C_i^P = C_i^L\,(a) + C_i^R\,(1–a) \text{ or}$$
$$C_i^P – C_i^R = a\,\left(C_i^L – C_i^R\right)$$

where C_i is the concentration of element i in L, R or P; and a is the mass fraction of extracted liquid. The differences ($C_i^P - C_i^R$) against ($C_i^L - C_i^R$) for major elements are plotted in Fig. 15. They fit to a regression line whose slope (m) is the mass fraction of liquid (a):

$$a = m = \left(C_i^P – C_i^R\right)/\left(C_i^L – C_i^R\right)$$

Major element data i in the mixture exhibit a regular linear trend. The overall correlation of the three rocks that extract a liquid mass fraction of 0.59 has a Pearson (R2) coefficient of around 99%, which is considered good for SiO_2, MgO, Fe_2O_3, MnO, and CaO and moderate for Al_2O_3. Discrepancies are higher for Na_2O and K_2O, and their unbalance can be due to the loss of these elements due to the fact that they are mobile elements. This high correlation reinforces the hypothesis that leucogranites formed as near-solidus liquids from the melting of an upper metapelitic crust leaving a granulitic residue that represents the composition of the lower crust.

	L	R	P
SiO_2	73.70	43.93	61.33
TiO_2	0.16	1.50	0.84
Al_2O_3	14.23	24.90	18.41
Fe_2O_3T	1.48	14.66	7.11
MgO	0.42	5.89	2.60
MnO	0.03	0.20	0.08
CaO	0.94	1.33	1.16
Na_2O	3.56	1.60	2.31
K_2O	4.63	0.75	3.50

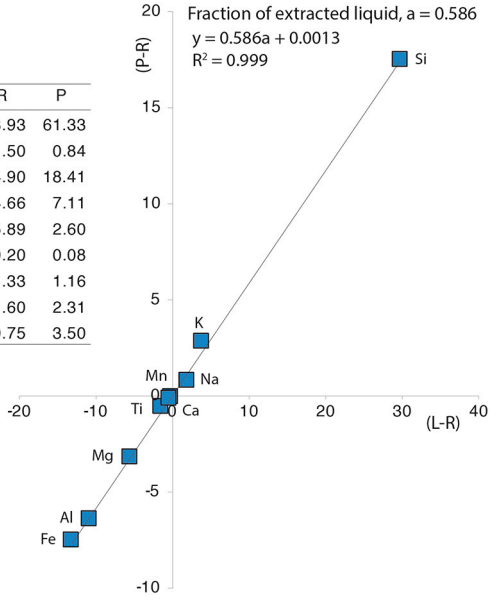

Fig. 15. Mass balance plot of a mixture of two end member compositions: leucogranite (L) and restitic melanosome (R). A mixture with a mass fraction of liquid (leucogranite) of 59% fits with the composition of metapelites from the area, which represent the protolith (P). Major elements plot very close to the regression line, satisfying the equation of a straight line.

7.3. Water content of magmas

The amount of water dissolved in the magmas at the time of emplacement and the crystallization of SL–LJ granitoid, mafic complexes and leucogranites can be estimated through several approaches. For SL–LJ granitoids the hydrated character of magmas is revealed by the presence of hornblende and biotite. However, pegmatitic textures are absent and the only evidence for water saturation is the presence of scarce miarolitic textures at the top of the porphyritic monzogranite, which represent the earliest, most evolved and shallowest magmas. This indicates that SL–LJ magmas were dominantly water under-saturated. According to Scaillet et al. (1998), granitic magmas must have around 4–6 wt% H_2O at emplacement. Phase equilibria experiments with I-type granodiorites indicate that a minimum of 2.5 wt% initial water is required at 0.8 GPa to stabilize hornblende, postdating plagioclase in the crystallization sequence (Naney, 1983).

In the mafic complexes, the crystallization of amphibole, both in the ultramafic cumulates and mafic rocks, shows that the magma forming them was hydrated, whereas no textures indicative of saturation are observed. The polycrystalline amphibole clots in mafic rocks represent reaction products that pseudomorph early orthopyroxene (Naney, 1983), thus constraining the low water content of the magma during early crystallization. According to experimental data (Naney, 1983), the stability field of amphibole widens at higher pressure. In subsaturated granodioritic systems, amphibole forms a liquidus phase at high pressure (around 0.8 GPa) and temperature (around 1000–800 °C) and between 5 and 12 wt% water, whereas at lower water contents (3–5 wt%) it coexists with orthopyroxene (Naney, 1983). For the diorite pseudosection (Sample 566, Fig. 13), the estimated amount of water that matches petrographic observations and mineral composition is 1.1 wt%. This is consistent with observations by Scaillet et al. (1998), who showed that for diorites the water content of the crystallizing rock must be around 1.1 wt% H_2O.

Coarse-grained pegmatites locally occur related to leucogranites, indicating high water content in leucogranitic magmas, occasionally reaching saturation. Water in leucogranites likely can derive from dehydration-melting reactions mostly in metapelites and to minor extent in orthogneisses that took place during D2 or late-D2.

7.4. Possible sources of magmas and relationships between them

Rocks from the Mas Claret mafic complex have a clear mantle origin based on their mafic character, presence of ultramafic cumulates, and Sr and Nd isotope ratios ($^{87}Sr/^{86}Sr_i$ as low as 0.703774 and εNd_i as radiogenic as 0.7) as already suggested by Vilà et al. (2005). Their hydrated character, as evidenced by the presence of amphibole in both the mafic and ultramafic rocks, combined with LILE enrichment relative to HFSE suggests that the mantle was metasomatized by subducted materials. Low Sr/Y and no depletion of HREE marks the absence of garnet as a residual phase in the mantle source. However, this does not necessarily imply a shallow origin, as subduction-related mantle metasomatism may change the nature of the main aluminum-bearing phase within the typical garnet stability field, while amphibole or phlogopite stabilize (e.g., Sudo and Tatsumi, 1990). The source of the SL–LJ and Ceret rocks is more difficult to constrain given their more evolved character and higher crustal component. A metasomatized mantle component must be present according to the presence of amphibole in the mafic and ultramafic rocks of Ceret complex and in the tonalites and granodiorites from SL–LJ. Two main hypotheses may be considered: 1) differentiation of melts derived from subduction-metasomatised mantle (Cordilleran-type

magmas) and 2) partial melting of the lower crust triggered by underplating of mantle-derived mafic magmas (Caledonian-type magmas).

Hypothesis 1. Differentiation of mantle-derived magmas.

SL–LJ granitoids and Ceret gabbro-diorites may derive from assimilation and fractional crystallization processes from melts derived from a subduction mantle that have primitive basaltic to andesitic compositions (Lee et al., 2007; primary, according to Castro, 2020). Their magnesian composition (Fig. 6a, Miyashiro, 1970), together with the hydrated character support this hypothesis (Frost and Lindsley, 1991). However, they need a larger crustal contribution compared to Mas Claret magmas in order to explain their composition. This may be acquired by two main mechanisms: by a higher contribution of subduction-derived components or by stagnation of ascending mantle magmas in the lower crust. Regarding the higher contribution of subduction-derived components, and given the largely immobile character of Nd in aqueous fluids, mantle metasomatism by slab-derived partial melts was proposed as a source by which to introduce Nd into the mantle (Schmidt and Poli, 2003). Melting of subducted mélanges such as altered oceanic crust and sediments has also been suggested as a source of primitive melts of a more felsic initial composition (dioritic/andesitic) (Marschall and Schumaker, 2012), which may metasomatize the overlying mantle. This hypothesis is based on thermomechanical models that predict the formation of Rayleigh-Taylor instabilities in the subduction channel and the formation of siliceous diapirs, which intrude in the supra-subduction mantle wedge (Gerya et al., 2004). On the other hand, a crustal signature may be acquired by stagnation of ascending mantle magmas at, usually, lower crustal levels. The composition of high-Zr diorite, clearly reflecting crustal assimilation, supports this mechanism, which is also possible for regular-Zr and SL–LJ granitoids given their similar isotopic compositions.

Hypothesis 2. Lower crust partial melting.

Vilà et al. (2005) suggest that the magmas which formed SL–LJ were generated by partial melting of metatonalites in the lower crust. Underplating is a common mechanism when rheological and tectonic constraints preclude the ascent of mantle-derived magmas through the crust. Heat transfer may induce lower crust partial melting (Wickham and Oxburgh, 1987), which can be favoured if coupled with fluid transfer from hydrated mafic magmas into the overlying crust, lowering its solidus temperature (Castro, 2020). For instance, a pargasite-bearing, metasomatized mantle can melt by adiabatic decompression to produce sanukitoid magmas (Castro, 2020). The magma can be then emplaced in the deep granulitic lower crust (Castro, 2019), which is favoured by the strong mechanical contrast between a brittle mantle lithosphere and a more ductile continental lower crust. The underplated sanukitoid magma transfers heat and fluid, thus fertilizing the lower crust. As a consequence, granodioritic-tonalitic magma is formed. The isotopic signature of the sanukitoid magma can be transferred to the newly formed melt if the time that elapsed between different episodes of magmatism is short enough (ca. 5 Ma; Castro, 2020). In the Iberian massif (CIZ), Variscan sanukitoid magmas are represented as intrusions that are coeval with old and young granodiorite plutons; conversely, in the Pyrenees, sanukitoid magmas have only been cited in younger intrusions (ca. 290–300 Ma; Cap de Creus, Druguet et al., 2014).

This mechanism can thus account for the formation of primitive intermediate hydrated magmas from the lower crust, similar to those feeding the SL–LJ pluton. In this scenario, production of more mafic magmas like those of Ceret and Mas Claret would be more difficult. Instead, these may represent magmas derived from the original underplating mantle magmas that were modified by assimilation and fractional crystallization processes. Assimilation of restitic materials by high-Zr diorites supports interaction with previously melt-depleted lower crustal materials. Large assimilation of lower crustal materials by Ceret magmas also explains its similar, but not equal, isotopic composition to SL–LJ magmas. Regarding the nature of the lower crust involved, HREE content in SL–LJ rocks indicates that garnet was not a residual phase. Additional work is needed in order to further discern between the mantle or crustal origin of SL–LJ magmas.

7.5. Magmatic history

The oldest magmas in the study area are those which produced the SL–LJ pluton. The first magmatic pulse corresponded to the emplacement of the porphyritic monzogranite located at the roof of the pluton (Fig. 14a). It intruded at a shallow depth as shown by the miarolitic cavities. This first pulse was followed by a larger and more continuous magma input, which built most of the current SL–LJ body. A single long-lived magmatic event for this second pulse is established by the granodiorite-tonalite zonation and by the absence of contacts between them (Fig. 14b). A density gradient within the magma chamber could be partly responsible for the tonalite – granodiorite – granite layering from the bottom to the top of the pluton. By the time this second magma pulse occurred, the monzogranite was already cold, at least at its border, as demonstrated by the porphyritic cooling facies of the granodiorite against it. In the tonalite, magma flow was registered during the first stages of crystallization by the magnetic fabric of biotite and hornblende (Olivier et al., 2016) as well as by the preferred orientation of plagioclase prisms that are roughly parallel to the outer contacts (Fig. 2a) providing evidence for a high degree of partial melting upon emplacement. Complex zircon growth from 314 ± 1.5 Ma (age of Zr cores in a tonalite) to 311 ± 0.9 Ma (age of rims) reflect the long residence time of SL–LJ magmas in the lower crust prior to emplacement and solidification at shallower levels. Diorite enclaves within the tonalite may represent either the more mafic compositions of SL–LJ magma in the deep reservoir or small intrusions of the underplating mafic magma into the reservoir.

Ceret magmas are unlikely to represent the most primitive types of SL–LJ magma based on major and trace element as well as isotope chemistry. Instead, they may represent either remnants of underplating mafic magmas, or newly formed mantle magmas produced by adiabatic ascent related to local extensional tectonics. Similarly to SL–LJ pluton, their high crustal component suggests a relatively long crustal-residence time, which is supported by the range of zircon age (from 312 ± 1.6 Ma in the core to 307.6 ± 1.5 Ma in the rim, Aguilar et al., 2014). Their ascent after the emplacement of the SL–LJ pluton may be favoured by the emptying of the overlying intermediate magma reservoir, which had previously acted as a mechanical and density barrier. Overlap of the oldest ages obtained in the zircon cores for the Ceret mafic magma (312 ± 1.6 Ma Ma; Aguilar et al., 2014) with those from a SL–LJ tonalite (314 ± 1.5 Ma; Aguilar et al., 2014) support the coexistence of both magmas at the lower crustal levels, and thus the underplating character of Ceret magmas. Contrary to Ceret magmas, the more preserved mantle composition of Mas Claret rocks with minor crustal influence indicates a faster ascent through the crust. Mas Claret magmas therefore likely formed by adiabatic decompression melting of the subduction-metasomatized mantle, which was favoured by the strike-slip extensional regime. Prior to that time, compressional tectonics and rheological constrains precluded the ascent of magmas with mafic or intermediate compositions. Additionally, Mas Claret (and to a much lower degree Ceret) magmas underwent shallow level fractional crystallization which produced the ultramafic cumulates.

Leucogranites were the last magmas to intrude. Their genesis by partial melting of the intermediate crust was triggered by regional conditions that reached anatexis of metapelitic rocks and were favoured by the additional heat provided by the emplacement of mafic magmas. They were either emplaced in situ, linked with the migmatitic rocks, or they were uprooted, cutting both the previously intruded igneous rocks and the country rocks. Nevertheless, minor interaction and local ductile deformation at the intrusive contacts indicate that at least a part of the SL–LJ pluton and the mafic complexes were not completely solidified when the leucogranites intruded.

Regardless of whether a mantle or a crustal origin for the genesis of magmatism is considered in the study area, both processes involve a subduction-metasomatized mantle magma component that formed in a supra-subduction environment. In a compressive setting such as the prevailing before the initial emplacement of the SL–LJ pluton (during D1), partial melting in the mantle requires either an active subduction or mantle upwelling by lower crust delamination. The SL-LJ magmas emplaced in a *syn*-collisional environment, and thus after subduction. However, according to thermomechanical models of subduction zones (Vogt et al., 2013) there may be a delay of several tens Myr between the end of ocean closure preceding continental collision and the emplacement of subduction-derived magmas. In the western European Variscan hinterland, the intrusion of most calc-alkaline plutons generally postdates subduction by more than 40 Ma (Castro, 2019) and this may also be the case of the SL–LJ pluton. The large volume (at least 2300 km^3) of SL–LJ magmas may have accumulated in the lower crust for millions of years during ongoing subduction due to either continuous underplating-related crustal melting or mantle magma supply, which produced the growth of the magma reservoir. On the other hand, delamination processes are typically associated to crustal thickening, mainly during continental collision. During delamination, mantle upwelling results in adiabatic decompression and partial melting. Partial melting of hydrated, pargasite-bearing subduction-metasomatized mantle produces magmas similar in composition to those derived from active subduction, thus making differentiation between them difficult. In addition, both the ascent of deeper hotter mantle and the underplating by mantle-derived magmas result in an increased thermal gradient at the new base of the crust which may favour its partial melting. All the argued models for the origin of magma consider magma accumulation at the lower crust. Compressional tectonics and rheological constrains precluded the ascent of magmas with mafic or intermediate compositions. During the period of magma accumulation and reservoir growth, continuous magma and/or heat supply likely maintained a molten state which favoured elemental and isotopic homogenization and hampered magma differentiation.

Upon continental collision, after cessation of underplating or mantle magma input (due to continental collision and subduction end in the subduction model, or to upwelled mantle equilibration in the delamination model), such a large volume of magma may have remained partially melted a long time, evolving by fractional crystallization processes until a part of the magma reservoir reached monzogranitic composition. This magma would have been buoyant enough to ascend through the overlying crust to produce the first and shallowest intrusion of the SL–LJ pluton, the porphyritic monzogranite, located at its roof (Fig. 14a), while the more mafic and denser magma remained in the lower reservoir.

Alternatively, the increasing influence of the mantle melts during the magmatic evolution, as revealed by the geochemical data presented in this paper, suggests delamination of the overriding plate (as suggested by Laurent et al., 2017). Delamination would inhibit crustal thickening and would occur at the late stages of the Variscan orogeny in the transition from a prevailing contractional (or transpressional) regime to a strike-slip or extensional regime. This transition would favour heat transfer from the mantle and decompression melting of hydrated, pargasite-bearing mantle peridotite. Thus, it would trigger the ascent of magmas accumulated in the lower crust during the previous compressional tectonic episodes, as well as of newly formed mantle-derived magmas likely generated by delamination-related mantle upwelling, such as those from the mafic complexes. Delamination would also explain the thermal evolution of the deeper levels with dome formation, decompressive P-T-t paths and the coeval development of late-Variscan extensional basins at upper crustal levels with calc-alkaline magmatism.

Other authors proposed a dextral transpressive setting for the emplacement of plutons during Late Variscan times (e.g., Antolín-Tomás et al., 2009; Carreras and Druguet, 2014; Denèle et al., 2009; Laumonier et al., 2010; Leblanc et al., 1996). Some of the transpressive models suggest strain partitioning between lower and upper structural levels with eastward flow of lower structural levels during metamorphic doming, coeval to thickening of the upper crust (Cochelin et al., 2017). Nevertheless, the decompressive *P–T* paths of metamorphic and magmatic rocks are hardly compatible with this setting. The transpressive setting is also not consistent with the coeval emplacement of plutons at depth and extensional volcano-sedimentary basins at upper crustal levels (Lloret et al., 2018; Pereira et al., 2014). A transpressional setting could prevail at the early stages of delamination but could not further continue as decoupling and delamination continued at late-Variscan times. The association of strike-slip faults and shear zones as growth mechanisms of granite plutons has been suggested for the Extremadura pluton as well (Castro and Fernández, 1998) and the Cabeza de Araya pluton (Vigneresse and Bouchez, 1997), among other areas. A strike-slip tectonic setting during pluton emplacement constitutes the transition from ductile processes to brittle extensional tectonics that took place at the end of the Variscan orogeny, as reported elsewhere along the belt (Tomek et al., 2019). The proposed tectono-magmatic relationships are also consistent with the Late Variscan (mainly Permian) dextral Intra-Pangea shear zone and to a set of shear zones along the Variscan belt related to the westward movement of Gondwana with respect to Laurasia (Berra and Angiolini, 2014) in addition to the coeval extensional orogenic collapse (Tomek et al., 2019). This dextral system would then merge into the subduction zone at the northern edge of the Paleo-Tethys, which continued subducting underneath Laurasia westward of Adria.

8. Conclusions

The Sant Llorenç – La Jonquera (SL–LJ) pluton constitutes a syn- to post-collisional sheet-like intrusive body of more than 290 km^2. The antiformal shape of the studied area provides the outcrop of a thick crustal section with a wide spectrum of magmatic rocks forming three suites: (1) the SL–LJ intrusion composed of quartz diorite, tonalite, granodiorite and monzogranite; (2) the Mas Claret and Ceret mafic complexes constituted by gabbro-diorite including ultramafic cumulates; (3) leucogranite dykes crosscutting the former rocks (Fig. 1b). The SL–LJ complex is part of a set of Variscan intrusions cropping out in the Pyrenees (Fig. 1a), Catalan Coastal Ranges, Variscan Iberian Massif, and French Central Massif. The magmatic association can be classified as magnesian, calc-alkaline, and metaluminous to slightly peraluminous and it is characteristic of active margins and post-collisional plutons of Caledonian type (I-type granite).

Amphibole and biotite are the dominant mafic phases of the SL–LJ intrusion and mafic complexes, thus indicating that the rocks formed from a parental undersaturated water-bearing magma of intermediate composition. The magma forming the mafic complexes derived from melting of an ultramafic source in a metasomatized supra-subduction mantle. This magma was variably contaminated by deep continental crustal rocks of intermediate composition, with the Mas Claret complex showing the most primitive compositions and the Ceret complex the most contaminated ones, including a suite of high Zr and Fe garnet-bearing magma. The origin of SL–LJ magmas is related either to large crustal contamination of mantle-derived magmas or to underplating-triggered lower crustal melting. The latter case would be related to mantle-derived sanukitoid magmas emplaced in between the more rigid mantle and the ductile lower crust favoured by their rheological contrast. The fluid from the sanukitoid magma fertilized the lower crust and a great volume of magma of intermediate composition was produced.

The origin of SL–LJ magmas is related either to large crustal contamination of magmas derived from subduction-metasomatized mantle, or to underplating-triggered lower crustal melting. The latter case would be related to mantle-derived sanukitoid magmas emplaced in between the more rigid mantle and the ductile lower crust favoured by their rheological contrast. The fluid from the sanukitoid magma

fertilized the lower crust and a great volume of magma of intermediate composition was produced. In either case, mantle-derived magmas would have formed related to active subduction or lower crust delamination.

A large isotopically homogeneous magmatic reservoir formed at the lower crust prior to final differentiation, ascent and emplacement of the SL–LJ magma. Leucogranite magma formed by anatexis of middle crustal rocks, similar in composition to that of metapelites and orthogneisses cropping out in the area.

All magmas in the studied area evolved by crustal assimilation and crystal fractionation in distinct magma pulses. SL–LJ granitoids, magnesian mafic rocks and leucogranite fractionated plagioclase thus indicate low pressure melts. In ferroan garnet-bearing mafic rocks, garnet was an early deep phase in equilibrium with Fe—Mg amphibole, thereby accounting for high pressure melts at around 0.75 GPa. A retrograde decompression path down to 0.55 GPa at a temperature over 700 °C was modelled for a crystallizing garnet-bearing diorite.

The deduced magmatic evolution as well as the structural and geometric relationships between the SL–LJ sheet and country rocks record the transition from a contractional or transpressional tectonic regime, characterized by crustal thickening, to a strike-slip regional setting that occurred during lithospheric delamination of the upper plate at late Variscan times, prior to the extensional collapse of the orogen and the breakup of Pangea. An initial emplacement of the monzogranite from the SL–LJ plutonic complex was followed by a single long-lived magmatic pulse that formed the rest of the sheet. The strike-slip tectonic regime characterized by the coexistence of extensional faults and contractional features (anticlines and domes) promoted the subsequent ascent and emplacement of the mafic complexes and leucogranites as favoured by decompression melting of a previously thickened continental crust. The magma intruded in successive pulses into the progressively created space as faults developed. This tectonic setting is consistent with the Late Variscan Intra-Pangea shear zone all along the entire contact between Laurasia and Gondwana.

Supplementary data to this article can be found online at https://doi.org/10.1016/j.lithos.2021.106541.

Author contributions

ML: responsible for the paper, ensuring that the descriptions are accurate and agreed by all authors. All authors have critically reviewed the manuscript and contributed to different parts of it. **ML**, **CA**: Conceptualization, methodology, geochemistry, pseudosection modeling, original draft preparation, visualization of figures, graphs and tables, writing - **AC:** Conceptualization, methodology, geochemistry, graphs and tables, writing - **GG**: Geochemistry, graphs and tables, writing - **JR**: Pseudosection modeling, writing - **MV**: critical review of the manuscript - **JAM**: Structure and regional tectonic framework of magmatism, writing.

Declaration of Competing Interest

The authors declare that they have no known competing financial interests or personal relationships that could have appeared to influence the work reported in this paper.

Acknowledgements

This work was benefited from the Spanish Commission for Science and Technology research projects CGL2015-66335-C2-2-R, PGC2018-096534-B-I00 (IBERCRUST) and PGC2018-093903-B-C22. It has also been financed by PID2020-117332GB-C21, PID2020-117332GB-C22, PID2019-109018RB-I00 and PID2020-117598GB-I00, funded by MCIN/AEI /10.13039/501100011033. C. Aguilar is indebted to prof. K. Schulmann and P. Sipska from the *Centre for Lithospheric Research, Czech Geological Survey* for their guidance and support over the past few years. We are also grateful to the technicians from the CCiTUB of the University of Barcelona and from the University of Granada for their help with X-ray fluorescence and coupled induction plasma operating. English language revised by Grant George Buffett (www.terranova.barcelona). We thank Yoann Denèle and an anonymous referee for critical review of the manuscript, which helped improve it. We also appreciate the work of Greg Shellnutt, Co-Editor-in-Chief of this journal.

References

Aguilar, C., Liesa, M., Castiñeiras, P., Navidad, M., 2014. Late-Variscan metamorphic and magmatic evolution in the Eastern Pyrenees revealed by U–Pb age zircon dating. J. Geol. Soc. Lond. 171, 181–192. https://doi.org/10.1144/jgs2012-086.

Aguilar, C., Liesa, M., Štípská, P., Schulmann, K., Muñoz, J.A., Casas, J.M., 2015. P–T–t–d evolution of orogenic middle crust of the Roc de Frausa Massif (Eastern Pyrenees): A result of horizontal crustal flow and Carboniferous doming? J. Metamorph. Geol. 33, 273–294.

Aguilar, C., Liesa, M., Reche, J., Powell, R., 2016. Fluid-fluxed melting and melt loss in a syntectonic contact metamorphic aureole from the Variscan Eastern Pyrenees. J. Metamorph. Geol. 34, 379–400.

Antolín-Tomás, B., Román-Berdiel, T., Casas-Sainz, A.M., Gil-Peña, I., Oliva, B., Soto, R., 2009. Structural and magnetic fabric study of the Marimanha granite (Axial Zone of the Pyrenees). Int. J. Earth Sci. 98, 427–441. https://doi.org/10.1007/s00531-007-0248-1.

Arranz, E., 1997. Petrología del macizo granítico de La Maladeta (Huesca-Lérida): estructura, mineralogía, geoquímica y petrogénesis. Unpublished PhD thesis. Universidad de Zaragoza, Zaragoza.

Baudin, T., Autran, A., Guitard, G., Laumonier, B., 2009. Carte géologique de la France a 1/50.000. In: Baudin, T., Autran, A., Laumomier, B., Calvet, M. (Eds.), Feuille Arles-sur-Tech (1100), Notice explicative par. BRGM, Orléans.

Berra, L., Angiolini, F., 2014. The evolution of the Tethys region throughout the phanerozoic: A brief tectonic reconstruction. In: Marlow, L., Kendall, C., Yose, L. (Eds.), Petroleum Systems of the Tethyan Region: AAPG Memoir, vol. 106, pp. 1–27. https://doi.org/10.1306/13431840M1063606.

Brophy, J.G., 1991. Composition gaps, critical crystallinity, and fractional crystallization in orogenic (calc-alkaline) magmatic systems. Contrib. Mineral. Petrol. 109, 173–182. https://doi.org/10.1007/BF00306477.

Capitani, C., Petrakakis, K., 2010. The computation of equilibrium assemblage diagrams with Theriak/Domino software. Am. Mineral. 95 (7), 1006–1016. https://doi.org/10.2138/am.2010.3354.

Carreras, J., Druguet, E., 2014. Framing the tectonic regime of the NE Iberian Variscan segment. Geol. Soc. Spec. Publ. 405 (1), 249–264.

Castiñeiras, P., Navidad, M., Liesa, M., Carreras, J., Casas, J.M., 2008. U–Pb zircon ages (SHRIMP) for Cadomian and Early Ordovician magmatism in the Eastern Pyrenees: New insights into the pre-Variscan evolution of the northern Gondwana margin. Tectonophysics 461, 228–239.

Castro, A., 2013. Tonalite-granodiorite suites as cotectic systems: A review of experimental studies with applications to granitoid petrogenesis. Earth-Sci. Rev. 124, 68–95.

Castro, A., 2019. An overview on the petrogenesis of the large batholiths and the mantle-related, basic and intermediate rocks. In: Quesada, C., Oliveira, J.T. (Eds.), The Geology of Iberia: A Geodynamic Approach. Vol. 2: The Variscan Cycle. https://doi.org/10.1007/978-3-030-10519-8.

Castro, A., 2020. The dual origin of I-type granites: the contribution from laboratory experiments. Geol. Soc. Lond., Spec. Publ. https://doi.org/10.1144/SP491-2018-110.

Castro, A., 2021. A non-basaltic experimental cotectic array for calc-alkaline batholiths. Lithos 382–383 (2021), 105929. https://doi.org/10.1016/j.lithos.2020.105929.

Castro, A., Fernández, C., 1998. Granite intrusion by externally induced growth and deformation of the magma reservoir, the example of the Plasenzuela pluton, Spain. J. Struct. Geol. 20, 1219–1228.

Clarke, D.B., 1981. The mineralogy of peraluminous granites: a review. Can. Mineral. 19, 3–17.

Clarke, D.B., Rottura, A., 1994. Garnet-forming and garnet-eliminating reactions in a quartz diorite intrusion at Capo Vaticano, Calabria, Southern Italy. Can. Mineral. 32, 623–635.

Cochelin, B., Chardon, Dominique, Denèle, Y., Gumiaux, C., Le Bayon, B., 2017. Vertical strain partitioning in hot Variscan crust: syn-convergence escape of the Pyrenees in the Iberian-Armorican syntax. Bulletin de la Société Géologique de France 188, 39. https://doi.org/10.1051/bsgf/2017206.

Cocherie, A., 1984. Interaction manteau–croûte: son rôle dans la génèse d'associations plutoniques calco-alcalines, contraintes géochimiques (élements en traces et isotopes du strontium et de l'oxygène). PhD thesis. Université de Rennes. Éditions du BRGM, 246 pp.

Couzinié, S., Moyen, J.-F., Villaros, A., Paquette, J.-L., Scarrow, J.H., Marignac, C., 2014. Temporal relationships between Mg-K mafic magmatism and catastrophic melting of the Variscan crust in the southern part of Velay Complex (Massif Central, France). J. Geosci. 59, 69–86.

Cruden, A.R., McCaffrey, K.J.W., 2001. Growth of plutons by floor subsidence: implications for rates of emplacement, intrusion spacing and melt-extraction mechanisms. Phys. Chem. Earth Solid Earth Geod. 26, 303–315.

Debon, F., Le Fort, P., 1983. A chemical-mineralogical classification of common plutonic rocks and associations. Trans. R. Soc. Edinb. Earth Sci. 73, 135–149. https://doi.org/10.1017/S0263593300010117.
Debon, F., Le Fort, P., 1988. A cationic classification of common plutonic rocks and their magmatic associations: principles, method, applications. Bull. Mineral. 111-5, 493–510.
Debon, F., Enrique, P., Autran, A., 1995. Magmatisme hercynian. In: Barnolas, A., Chiron, J.C. (Eds.), Synthèse géologique et géophysique des Pyrénées, Introduction. Géophysique, vol. 1.
Denèle, Y., Olivier, Ph., Gleizes, G., Barbey, P., 2009. Decoupling between the middle and upper crust during transpression-related lateral flow: Variscan evolution of the Aston gneiss dome (Pyrenees, France). Tectonophysics 477, 244–261.
Denèle, Y., Barbey, P., Paquette, J.-L., Laumonier, B., Olivier, Ph., 2012. Time scale of gneiss dome formation and ductile flow: the Mont-Louis, Ax-les-Thermes and La Jonquera plutons and related gneiss domes in the French Pyrenees. Géol. Fr. 1, 101–102.
Druguet, E., Castro, A., Chichorro, M., Pereira, M.F., Fernández, C., 2014. Zircon geochronology of intrusive rocks from Cap de Creus, Eastern Pyrenees. Geol. Mag. 151, 1–20. https://doi.org/10.1017/S0016756814000041.
Estévez, A., 1973. La vertiente meridional del Pirineo Catalán al N del curso medio del Río Fluviá. Ph.D. Universidad Granada, 514 pp.
Evensen, N.M., Hamilton, P.J., Onions, R.K., 1978. Rare-Earth abundances in chondritic meteorites. Geochim. Cosmochim. Acta 42, 1199–1212.
Faure, G., Mensing, T.M., 2005. Isotopes. Principles and Applications, 3rd ed. John Wiley & Sons, Inc, Hoboken, New Jersey.
Frost, B.R., Lindsley, D.H., 1991. The occurrence of Fe-Ti oxides in igneous rocks. In: Lindsley, D.H. (Ed.), Oxide Minerals: Petrologic and Magmatic Significance, Mineralogical Society of America, Reviews in Mineralogy, 25, pp. 433–486.
Frost, B.R., Barnes, C.G., Collins, W.J., Arculus, R.J., Ellis, D.J., Frost, C.D., 2001. A geochemical classification for granitic rocks. J. Petrol. 42, 2033–2048.
Galán, G., Enrique, P., Butjosa, L., Fernández-Roig, M., 2017. Spinels of Variscan olivine hornblendites related to the Montnegre granitoids revisited (NE Spain): Petrogenetic evidence of mafic magma mixing. Geol. Acta 15, 323–336. https://doi.org/10.1344/GeologicaActa2017.15.4.5.
Gerya, T.V., Yuen, D.A., Sevre, E.O.D., 2004. Dynamical causes for incipient magma chambers above slabs. Geology 32, 89–92.
Gisbert, J., 1984. Las molasas tardihercínicas del Pirineo. In: Comba, J.A. (Ed.), Geología de España. Libro Jubilar de J.M. Ríos, IGME, Madrid, pp. 168–186.
Hall, A., 1966. The Ardara pluton: a study of the chemistry and crystallisation of a contaminated granite intrusion. Proc. R. Ir. Acad. 65B, 203–235.
Hamilton, W., Myers, W.B., 1967. The nature of plutons. US Geol. Surv. Prof. Pap. 554-C, 1–30.
Hawthorne, F.C., Oberti, R., Harlow, G.E., Maresch, W.V., Martin, R.F., Schumacher, J. C., Welch, M.D., 2012. IMA report, nomenclature of the amphibole supergroup. Am. Mineral. 97, 2031–2048.
Holland, T.J.B., Powell, R., 2011. An improved and extended internally consistent thermodynamic dataset for phases of petrological interest, involving a new equation of state for solids. J. Metamorph. Geol. 29, 333–383.
Janoušek, V., Holub, F.V., Rogers, G., Bowes, D.R., 1997. Two distinct mantle sources of Hercynian magmas intruding the Moldanubian unit, Bohemian Massif, Czech Republic. J. Geosci. 42 (3), 10.
Laumonier, B., Marignac, C., Kister, P., 2010. Polymetamorphism and crustal evolution of the eastern Pyrenees during the Late Carboniferous Variscan orogenesis. Bulletin de la Société Géologique de France 181, 411–428.
Laurent, O., Couzinié, S., Zeh, A., Vanderhaeghe, O., Moyen, J.F., Villaros, A., Gardien, V., Chelle-Michou, C., 2017. Protracted, coeval crust and mantle melting during Variscan late-orogenic evolution: U–Pb dating in the eastern French Massif Central. Int. J. Earth Sci. 106 (2), 421–451. https://doi.org/10.1007/s00531-016-1434-9.
Leblanc, D., Gleizes, G., Roux, L., Bouchez, J.L., 1996. Variscan dextral transpression in the French Pyrenees: new data from the Pic des Trois–Seigneurs granodiorite and its country rocks. Tectonophysics 261, 331–345.
Lee, C.T.A., Morton, D.M., Kistler, R.W., Baird, A.K., 2007. Petrology and tectonics of Phanerozoic continent formation: from island arcs to accretion and continental arc magmatism. Earth Planet. Sci. Lett. 263, 370–387.
Liesa, M., 1994. Relations of Hercynian metamorphism with magmatism and deformation in the Eastern Pyrenees. Implications for Hercynian evolution. Geol. Mijnb. 72, 295–304.
Liesa, M., Carreras, J., 1989. On the structure and metamorphism of the Roc de Frausa Massif (Eastern Pyrenees). Geodin. Acta 3, 149–161.
Liesa, M., Carreras, J., Castiñeiras, P., Casas, J.M., Navidad, M., Vilà, M., 2011. U-Pb zircon age of Ordovician magmatism in the Albera Massif (Eastern Pyrenees). Geol. Acta 9, 93–101.
Lloret, J., Ronchi, A., López-Gómez, J., Gretter, N., de la Horra, R., Barrenechea, J.F., Arche, A., 2018. Syn-tectonic sedimentary evolution of the continental late Palaeozoic-early Mesozoic Erill Castell-Estac Basin and its significance in the development of the Central Pyrenees Basin. Sediment. Geol. 374, 134–157. https://doi.org/10.1016/j.sedgeo.2018.07.014.
López-Gómez, J., Arche, A., Pérez-López, A., 2002. Permian and Triassic. In: Gibbons, W., Moreno, T. (Eds.), The Geology of Spain. The Geological Society, London. https://doi.org/10.1144/GOSPP.10.
Marschall, H.R., Schumaker, J.C., 2012. Arc magmas sourced from mélange diapirs in subduction zones. Nat. Geosci. 5, 862–867.
Maurel, O., 2003. L'exhumation de la Zone Axiale des Pyrénées orientales: une approche thermo-chronologique multi-méthodes du rôle des failles. PhD thesis. Université de Montpellier II.
Miyashiro, A., 1970. Volcanic rock series in island arcs and active continental margins. Am. J. Sci. 274, 321–355.
Moyen, J.F., 2009. High Sr/Y and La/Yb ratios: the meaning of the "adakitic signature". Lithos 112, 556–574.
Muñoz, J.A., 1992. Evolution of a continental collision belt: ECORS Pyrenees crustal balanced cross-section. In: McClay, K.R. (Ed.), Thrust Tectonics. Chapman & Hall, London, pp. 235–246.
Muñoz, J.A., Martinez, A., Vergés, J., 1986. Thrust sequences in the eastern Spanish Pyrenees. J. Struct. Geol. 8, 399–405.
Naney, M.T., 1983. Phase equilibria of rock-forming ferromagnesian silicates in granitic systems. Am. J. Sci. 283, 993–1033.
Narduzzi, F., Farina, F., Stevens, G., Lana, C., Nalini Jr., H.A., 2017. Magmatic garnet in the Cordilleran-type Galiléia granitoids of the Araçuaí belt (Brazil): evidence for crystallization in the lower crust. Lithos 282–283, 82–97.
Olivier, P., Druguet, E., Castaño, L.M., Gleizes, G., 2016. Granitoid emplacement by multiple sheeting during Variscan dextral transpression: the Saint-Laurent – La Jonquera pluton (Eastern Pyrenees). J. Struct. Geol. 82, 80–92. https://doi.org/10.1016/j.jsg.2015.10.006.
Pereira, M.F., Castro, A., Chichorro, M., Fernández, C., Díaz-Alvarado, J., Martí, J., Rodríguez, C., 2014. Chronological link between deep-seated processes in magma chambers and eruptions: Permo-Carboniferous magmatism in the core of Pangaea (Southern Pyrenees). Gondwana Res. 25, 290–308.
Roberts, M.P., Pin, C., Clemens, J.D., Paquette, J.L., 2000. Petrogenesis of mafic to felsic plutonic rock associations: the calc-alkaline Quérigut complex, French Pyrenees. J. Petrol. 41, 809–844.
Scaillet, B., Clemente, B., Evans, B.W., Pichavant, M., 1998. Redox control of sulfur degassing in silicic magmas. J. Geophys. Res. B: Solid Earth 103, 23937–23949.
Scarrow, J.H., Molina, J., Bea, F., Montero, P., 2009. Withinplate calc-alkaline rocks: insights from alkaline mafic magma – peraluminous crustal melt hybrid appinites of the Central Iberian Variscan continental collision. Lithos 110, 50–64.
Schmidt, M.W., Poli, S., 2003. Generation of mobile components during subduction of ocean crust. In: Holland, H.D., Turekian, K.K. (Eds.), Treatise on Geochemistry, The Crust, Volume 3. Elsevier, Oxford, pp. 567–591.
Sinigoi, S., Quick, J., Demarchi, G., Klötzli, U., 2011. The role of crustal fertility in the generation of large silicic magmatic systems triggered by intrusion of mantle magma in the deep crust. Contrib. Mineral. Petrol. 162, 691–707. https://doi.org/10.1007/s00410-011-0619-2.
Soler, A., Enrique, P., 1989. La terminación sur-occidental del batolito de Andorra-Mont Lluís: características petrológicas y geoquímicas. Acta Geol. Hisp. 24, 139–146.
Soliva, J., 1992. Les déformations ductiles dans la zone axiale des Pyrénées orientales: La convergence varisque, la mise en place des granites tardi-hercyniens, la convergence pyrénéenne. Thèse Doct. Université Montpellier II, 186 pp.
Sudo, A., Tatsumi, Y., 1990. Phlogopite and K-amphibole in the upper mantle: Implication for magma genesis in subduction zones. Geophys. Res. Lett. 17, 29–32. https://doi.org/10.1029/GL017i001p00029.
Sun, W., McDonough, W.F., 1989. Chemical and isotopic systematics of oceanic basalts: Implications for mantle composition and processes. Geol. Soc. Lond., Spec. Publ. 42 (1) https://doi.org/10.1144/GSL.SP.1989.042.01.19.
Tomek, F., Vacek, F., Zák, J., Petronis, M.S., Verner, K., 2019. Polykinematic foreland basins initiated during orthogonal convergence and terminated by orogen-oblique strike-slip faulting: an example from the northeastern Variscan belt. Tectonophysics 766, 379–397. https://doi.org/10.1016/j.tecto.2019.05.023.
Vigneresse, J.L., Bouchez, J.L., 1997. Successive granitic magma batches during pluton emplacement: the case of Cabeza de Araya (Spain). J. Petrol. 38, 1767–1776.
Vigneresse, J.L., Tikoff, B., 1999. Strain partitioning during partial melting and crystallizing felsic magmas. Tectonophysics 312, 117–132.
Vilà, M., Pin, C., Enrique, P., Liesa, M., 2005. Telescoping of three distinct magmatic suites in an orogenic setting: Generation of Hercynian igneous rocks of the Albera Massif (Eastern Pyrenees). Lithos 83, 97–127.
Vilà, M., Pin, C., Liesa, M., Enrique, P., 2007. LPHT metamorphism in a late orogenic transpressional setting, Albera Massif, NE Iberia: implications for the geodynamic evolution of the Variscan Pyrenees. J. Metamorph. Geol. 25, 321–347.
Vogt, K., Castro, A., Gerya, T., 2013. Numerical modeling of geochemical variations caused by crustal relamination. Geochem. Geophys. Geosyst. 14, 470–487.
Voshage, H., Hofmann, A.W., Mazzucchelli, M., Rivalenti, G., Sinigoi, S., Raczek, I., Demarchi, G., 1990. Isotopic evidence from the Ivrea Zone for a hybrid lower crust formed by magmatic underplating. Nature 347 (6295), 731–736. https://doi.org/10.1038/347731a0.
Whitney, D.L., Evans, B.W., 2010. Abbreviations for names of rock-forming minerals. Am. Mineral. 95, 185–187.
Wickham, S.M., Oxburgh, E.R., 1987. Low pressure regional metamorphism in the Pyrenees and its implications for the thermal evolution of rifted continental crust. Philos. Trans. R. Soc. Lond. Ser. A 321, 219–243.